**UNIVERSITÀ DI PISA**
**Scuola di Dottorato in Ingegneria "Leonardo da Vinci"**


**Corso di Dottorato di Ricerca in**
**Ingegneria dell'Informazione**

**Tesi di Dottorato di Ricerca**

# UWB Analog Multiplier in 90nm CMOS SoC Pulse Radar Sensor for Biomedical Applications

***Martina Mincica***

***Anno 2011***
**SSD ING-INF/01**

**UNIVERSITÀ DI PISA**

**Scuola di Dottorato in Ingegneria "Leonardo da Vinci"**


**Corso di Dottorato di Ricerca in**
**Ingegneria dell'Informazione**

**Tesi di Dottorato di Ricerca**

# UWB Analog Multiplier in 90nm CMOS SoC Pulse Radar Sensor for Biomedical Applications

*Autore:*

*Martina Mincica* _____

*Tutori:*

*Prof. Danilo De Rossi* _____
*(University of Pisa)*

*Dr. Domenico Zito* _____
*(University College Cork and Tyndall National Institute)*

*Anno 2011*
SSD ING-INF/01

*Quando dire grazie non è necessario...*

## SOMMARIO

Questa tesi riporta la descrizione sintetica e i principali risultati dell'attività condotta nell'ambito del programma triennale (2008-2010) del dottorato di ricerca in Ingegneria dell'Informazione presso l'Università di Pisa. Il programma di ricerca è stato originato dal progetto europeo ProeTEX finalizzato allo sviluppo di una nuova generazione di attrezzature per gli operatori di emergenza, come pompieri e protezione civile.

In questo contesto, il gruppo di ricerca multidisciplinare nato dalla collaborazione internazionale dei gruppi di ricerca diretti dal Prof. Danilo De Rossi (Università di Pisa) per la Bio-ingegneria e dal Dr. Domenico Zito (University College Cork and Tyndall National Institute, Cork, Ireland) per la Microelettronica, si è occupato di realizzare un innovativo sensore radar ad impulsi ultra-wide-band (UWB) integrato su singolo chip in tecnologia CMOS per il monitoraggio senza contatto dell'attività cardio-polmonare. Questo sensore innovativo sarebbe così idoneo per essere utilizzato all'interno di una piattaforma tessile, pertanto indossabile, contenente altri sensori di parametri biologici. Il sensore radar è progettato per rilevare le frequenze cardiaca e respiratoria. Tali dati potrebbero essere disponibili per una trasmissione radio verso un personal server che coordina l'intera Wireless Body Area Network (WBAN). Un tale sistema radar ha il vantaggio di permettere un monitoraggio non invasivo e senza contatto col corpo. Inoltre esso rileverebbe direttamente l'attività meccanica del cuore invece di quella elettrica, così come avviene per un elettrocardiografo. La tecnologia radar UWB permetterebbe quindi un monitoraggio preliminare a basso rischio e senza contatto, superando i tradizionali limiti delle tecnologie esistenti (e.g. ultrasuoni).

In dettaglio, il radar trasmette una sequenza di brevi impulsi elettromagnetici verso il cuore e, grazie alla capacità delle microonde di penetrare i tessuti, rileva i movimenti del cuore correlando gli echi riflessi con le repliche locali opportunamente ritardate (tempo di volo) degli impulsi trasmessi.

L'argomento specifico del dottorato di ricerca, trattato in questa tesi, è stato la progettazione e la caratterizzazione del moltiplicatore analogico UWB realizzato in tecnologia CMOS 90nm. Si tratta di un blocco fondamentale nella catena di ricezione, responsabile della correlazione tra l'eco ricevuto (e amplificato) e la replica locale (generata on-chip) dell'impulso trasmesso. Il circuito completamente differenziale consiste di uno stadio differenziale p-MOSFET a gate comune in ingresso per ottenere l'adattamento a larga banda, uno stadio di moltiplicazione basato sulla cella di Gilbert a p-MOSFET e carichi attivi. Dato il limitato numero di lavori su multiplicatori analogici, è stata introdotta una nuova soluzione circuitale ed una nuova metrica utile per la progettazione e caratterizzazione nel dominio del tempo. Tale metrica permette di evidenziale il vero comportamento del sistema, diverso da quello di un tradizionale mixer che viene comunemente analizzato e testato nel dominio della frequenza. In dettaglio, la metrica introdotta, denominata Input-Output Energy Ratio (IOER), punta ad ottimizzare il progetto del circuito moltiplicatore di modo tale da massimizzare la tensione in uscita in corrispondenza di massima correlazione tra gli impulsi in ingresso.

La caratterizzazione sperimentale del circuito e il confronto con lo stato dell'arte hanno evidenziato che il moltiplicatore presenta uno dei migliori set di performance.

Il nuovo moltiplicatore è stato poi co-integrato assieme agli altri blocchi costituenti il sistema radar. Le verifiche sperimentali preliminari condotte dal gruppo di ricerca sull'intero radar, hanno confermato la validità dell'approccio. In particolare il sensore riesce a rilevare un target costituito da un foglio di cartone di spessore pari a 0.5 cm e superficie 26×26 $cm^2$ rivestito da un comune foglio di alluminio, fino a una distanza massima di 70 cm. Inoltre, il sensore radar è risultato essere in grado di rilevare il ritmo respiratorio di una persona posta ad una distanza di 25 cm. Questo lavoro presenta il primo sensore radar UWB funzionante, basato su correlator receiver, completamente integrato in tecnologia CMOS 90nm.

## ABSTRACT

This thesis reports the description and results of the doctoral research programme in Information Engineering (University of Pisa), carried out in the three years from 2008 to 2010. The doctoral research programme has been originated by the European project ProeTEX aimed at developing a new generation of equipments for the market of emergency operators, like fire-fighters and Civil Protection rescuers.

In this context, the multidisciplinary research group originated by the international cooperation of the research groups led by Prof. Danilo De Rossi (University of Pisa) as for Bio-engineering and Dr. Domenico Zito (University College Cork and Tyndall National Institute, Cork, Ireland) as for Microelectronics, has focused on the implementation of an innovative ultra-wide-band (UWB) pulse radar sensor fully integrated on a single silicon die for non-invasive and contact-less cardio-pulmonary monitoring within a wearable textile sensor platform. The radar sensor is designed to detect the heart and respiratory rates, which can be transmitted to a personal server that coordinates the entire Wireless Body Area Network (WBAN). Such radar sensor should sense the mechanical activity instead of the electrical activity of the heart. UWB bio-sensing allows low risk preliminary monitoring without discomfort since the radar system permits continuous monitoring without requiring any contact with the skin of the patient unlike the traditional technologies (i.e. ultrasounds).

In detail, the radar transmits a sequence of extremely short electromagnetic pulses towards the heart and, due to the capability of microwaves to penetrate body tissues, detects the heart wall movement by correlating the echoes reflected with local replicas of the transmitted pulses properly delayed (i.e. time of flight).

The specific aim of the doctoral research program has been the design and experimental characterization of the CMOS UWB analog multiplier, which is a crucial circuit in the receiver chain that implements the correlation between the received and amplified echo and the local replica, generated on-chip, of the transmitted pulse.

The fully-differential circuit consists of a p-MOSFET common-gate differential pair as input stage for a wideband impedance matching, a p-MOSFET Gilbert's quad as multiplier stage, and active loads. The circuit has been designed and fabricated in 90nm CMOS. Given the few works on similar analog circuits having inferior performance with respect to those requested, an innovative circuit solution has been delivered. Moreover, a novel time-domain metric has been introduced in order to put in evidence the real behaviour of the system that differs from a traditional mixer commonly analyzed using frequency-domain metrics. This new metric, namely Input-Output Energy Ratio (IOER), aims at the optimization of the multiplier circuit design so that the output voltage corresponding to maximum correlation between two input pulses is maximized.

The experimental characterization and the comparison with the state of the art have shown that the multiplier exhibits one of the best set of performance.

The novel multiplier has been co-integrated with the other building blocks of the radar. The preliminary experimental characterization of the test-chips carried out by the research group, has demonstrated that the proposed UWB radar sensor works properly. It can detect a reflective target consisting of a half-centimetre-thick board surface (26×26 $cm^2$) covered by aluminium foil up to a distance of 70 cm. Moreover, it can detect the respiratory rate of a person placed at a distance of 25 cm. This work presents the first implementation, including experimental evidences, of a SoC UWB pulse radar front-end based on a correlation receiver, in 90nm CMOS technology.

## OUTINE

## INTRODUCTION

Thanks to good life conditions in developed countries, the average life of population is continuously growing and consequently the incidence of chronic diseases [1]. Health science is a heterogeneous field, in which many different disciplines flow together in order to guarantee preventive and curative interventions through services that are supposed to be available and accessible on a large scale. Investments for innovation in this direction are huge and researchers are asked to find less and less expensive solutions to provide continuous and appropriate assistance to the millions of people suffering from chronic diseases, in large part associated with cardiovascular and pulmonary pathologies [2]. Innovative health assistance can be helpful also to rescue operators in mass fatalities and large disasters, in support of their own safety and consequently of their efficiency. One of the main issues of health assistance regards the enormous cost that every nation has to sustain in order to ensure it. The actual trend identifies Wireless Body Area Networks (WBANs) as the future of first-hand health monitoring and medical care [3]. A WBAN is a radio frequency RF-based wireless networking technology that interconnects tiny nodes with sensor or actuator capabilities in, on, or around a human body. In the last few years, many works related to WBANs and their realizations in different applicative scenarios have been published. Interesting solutions have been suggested in the field of physical rehabilitation [4], advanced health and disaster aid [5], and ambience intelligence [6]. Protocols and networking are already implemented in many of these works and many products, designed to be part of these networks, are already available on the market [7], [8], [9]. A relevant research is going on at networking level, but the real challenge is the evolution driven by the "disappearance" requirement for sensor nodes and in particular for sensors. The main issue remains the realization of a network capable of monitoring and interacting with a human body in an almost unnoticed way. On this point, the ever-shrinking standard microelectronic technology and the emerging micro-fabrication processes come into play allowing the integration of heterogeneous devices in a small physical volume [10].

In this world-wide framework, an international cooperation between the research groups led by Dr. Domenico Zito (University College Cork and Tyndall National Institute, Cork, Ireland) focused on system-on-chip implementation of nano-scale CMOS radio-frequency sensors for contact-less monitoring of primary physiological parameters and Prof. Danilo De Rossi (University of Pisa, Pisa, Italy) focused on the implementation of smart textile sensor platform for remote health monitoring, is addressed to the implementation of a new class of sensors for contact-less cardiopulmonary monitoring based on system-on-chip pulse radar. In fact, the opportunity of merging contact-less sensor into a wearable textile platform offers the interesting perspective of delivering an innovative enabling technology for advanced heart health wireless assistance, in response to the increasing needs of large scale and accessible medical service for monitoring the cardio-pulmonary chronic diseases of the population.

This research has been carried out within the large European project ProeTEX, particularly addressed to the bio-monitoring of rescue operators [11]. Details of the project context are presented in Chapter 1.

Originated by the research context above, the research reported in this PhD thesis has dealt with the design, implementation and characterization of a novel UWB CMOS analog multiplier, which is one of the critical building blocks of the system-on-chip radar proposed by the research group. Circuit description and experimental results will be presented in Chapter 2.

The UWB analog multiplier has been co-integrated with the other building blocks for the implementation of the entire system-on-chip radar. In order to further demonstrate the effectiveness of the novel analog multiplier, in Chapter 3, the preliminary (limited to respiratory rate) experimental results achieved for the system-on-chip radar recently carried-out with success by the research group is reported.

This thesis refers to the doctoral research programme carried out at the University of Pisa from its start in January 2008 up to August 2009, and at Tyndall National Institute (University College Cork) from September 2009 up to its completion in December 2010.

# 1. ENABLING TECHNOLOGY FOR HEART HEALTH WIRELESS ASSISTANCE

## *1.1 General aim of the work*

Several advances have been made in wireless body area networks for bio-monitoring, as confirmed by the fine tuning of ad-hoc standards for networking, controlling and managing a distributed sensor platform around the human body. Efficient wireless networks are becoming commercially available for several applications. In spite of that, sets of "invisible" sensors for monitoring bio-signals are still expected as enabling technology for mass-market applications.

The general objectives of this chapter consist in presenting the current state of the art and identifying some of the open challenges and requirements for the future heart health wireless assistance. The specific objective consists of presenting the contribution derived by the research project aimed at implementing an innovative contact-less miniaturized radar sensor for cardio-pulmonary monitoring within a wearable textile platform. In this specific framework, the technical context of the research project and its expected future extensions toward a full wireless textile platform, will be described. In detail, the chapter focuses on the realization of a low-cost, low-power, wearable and autonomous system for contact-less cardio-pulmonary monitoring. All these features are possible thanks to the System-on-Chip (SoC) integration of the sensor and wireless communication interface in deep submicron CMOS technology, within the textile sensor platform. In fact, the microchip capable of detecting heart and respiratory rates is thought to be co-integrated with an elasticized T-shirt so that the person under observation would not even notice its presence.

Both the contact-less cardio-pulmonary sensor and textile platform are developed within the European project ProeTEX addressed to the bio-monitoring of rescue operators [11].

In spite of this specific applicative context, the results of this research project can be extended to general textile platforms for WBANs. Considering the open challenges for public health assistance, this technology is expected to increase the quality of the medical service and reduce its costs.

The material presented in this chapter is reported in [12].

## *1.2 WBAN for bio-monitoring*

A WBAN for healthcare is a Wireless Sensor Network (WSN) with the specific intent of keeping a person under continuous health monitoring. It is an all-in-one implementation of what is called bio-monitoring. All sensors that create a WBAN are placed around, on or in the human body (see Fig. 1). The trend is to make these sensors smaller and smaller. The term "Smart Dust", referring to cubic millimeter-sized devices, is now just a concept, but in the future, molecular engineering and nanotechnology are expected to allow even smaller dimensions of a few cubic microns or maybe less [6].

### 1.2.1 WBAN sensors

There are some fundamental requirements that these sensors need to satisfy. They have to be low-cost, low-power, wearable, non-invasive and reliable. Consequently, their transmission range is expected to be quite short, usually less than two meters. This is one of the reasons why a WBAN is thought to be integrated in a Wireless Personal Area Network (WPAN), which can include many other devices [3]. The system managing all sensor nodes in a WBAN and other nodes in a WPAN is usually called Personal Server (PS) (see Fig. 1).

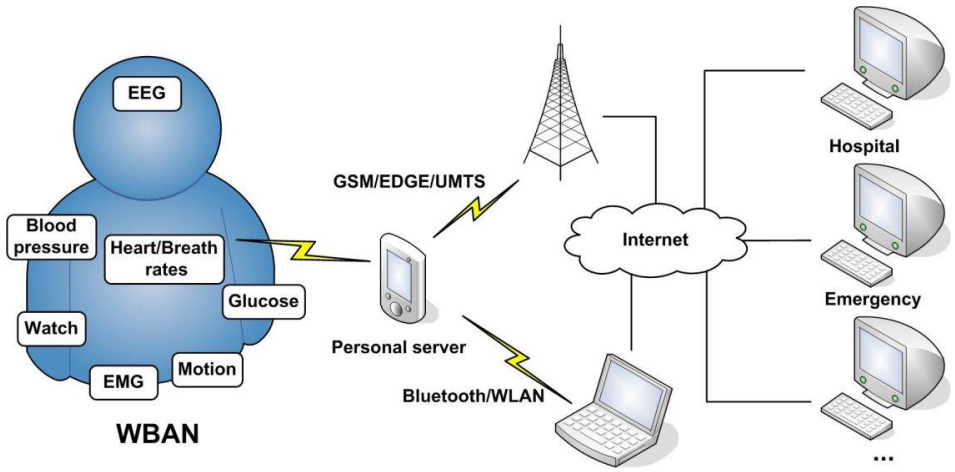


*Fig. 1 – WBAN for bio-monitoring with sensing platform controlled by a Personal Server and internet connectivity.*

The main target of health monitoring is to keep under control several markers of the human biology. A WBAN can include a large number of physiological sensors, which can be used as a bridge between the physical world and electronic systems, in order to generate all the information regarding the health status of the person under observation. There are a large number of sensors that are already commercially available:

- ECG (electrocardiogram) sensor for monitoring heart activity
- EMG (electromyography) sensor for monitoring muscle activity
- EEG (electroencephalography) sensor for monitoring brain electrical activity
- blood pressure sensor
- blood glucose sensor
- gyroscope and accelerometer for monitoring trunk position and movement
- breathing sensor for monitoring respiration
- infrared or diode-based sensors for monitoring temperature
- pulse oximeter for cardio-respiratory monitoring

### 1.2.2 Heart and respiration monitoring

This work focuses on heart and respiration monitoring as fundamental health markers in a human being. The analysis of heart rate (HR) and HR variability (HRV) is proven to be useful in understanding cardiovascular regulation in a wide range of conditions, including heart failure, diabetes, hypertension, and sleep

apnea [2, 13]. All these conditions are very frequent and affect a relevant part of the worldwide population as average life increases. The established way to check heart health consists of interpreting its electrical activity recorded by an Electrocardiography (ECG) over the observation time. This electro-medical device already exists in a portable size and it allows remote measurement and data report.

#### *1.2.2.1 Holter*

In particular, the clinical use of the telemetry for cardiac monitoring started in the early 1960s employing the Holter system, which can record signals from the heart (ECG) through a series of electrodes attached to the chest. A modem Holter system can monitor up to 72 hours by varying the sample rate [7]. However, to diagnose transient cardiac symptoms such as palpitations, chest pain, dizziness, syncope and shortness of breath that can indicate severe arrhythmias, a longer observation time is needed. Nowadays, Holter system is used to monitor patients with transient cardiac symptoms [8]. Such a system can almost be considered as part of a WBAN, except for its sensors. In fact, a Holter uses ECG electrodes placed on patient chest to detect the electrical heart activity. In [8] those electrodes are wired to a common necklace sensor node, where the information are stored, elaborated and transmitted by a wireless link to a small portable monitor (i.e. Personal Server), which re-transmits them to a storage centre where they can be processed and interpreted. Therefore, this device cannot be considered totally wearable and non-invasive.

#### *1.2.2.2 Pulse oximeter*

Another instrument of large clinical use is the pulse oximeter. This device measures the oxygen saturation of patient's blood and blood volume into the skin by illuminating the skin and measuring the light absorption. This is done by using LED (Light Emitting Diode) technology [14]. Pulse oximetry has become an important complementary system to monitor respiration and heart rate and there are several commercially available versions of these products, even wireless [9]. However, as all the other products currently on sale and previously mentioned for heart and respiration monitoring, it cannot be considered completely wearable and non-invasive, as a daily-used system for bio-monitoring is expected to be. Therefore, a sensor capable of detecting these vital parameters, in a way that is not perceived by the person under observation, is still missing. Microelectronic research is expected to provide innovative solutions in this relevant research space.

### 1.2.3 Contactless solutions in literature

In the last years the microelectronic research has been trying to achieve the realization of a completely wearable and non-invasive device that could be worn on a daily basis to detect vital parameters, in a way that is not perceived by the person under observation.

Microwave Doppler radar has been investigated to detect the respiration rate since 1975 [15]. Examples of application of pulse radars for the detection of vital parameters are reported in literature [16-18]. In spite of the differences, both the Doppler and pulse radars exploit the capability of microwaves to penetrate the human tissue layers (with unavoidable attenuation) and the reflection property of

the interface between two layers with different characteristic impedance (e.g. heart muscle and blood, in the case of the heart wall interface).

These first devices were implemented in hybrid technologies, resulting bulky and expensive, and then not responding to the needs described above. Thanks to the advances in microelectronics, a Continuous Wave (CW) Doppler radar capable of detecting heart and lungs movements was proposed in 2002 and 2004 [19, 20]. This represents the first attempt to implement the traditional hybrid-technology radars on silicon for medical use. Recently, other works based on the CW Doppler radar has been reported in the literature [21, 22].

Other techniques have been investigated to detect the vital parameters. A near infra-red sensor is presented in [23], an accelerometer sensor in described in [24] and an ultrasonic remote monitor and is application are shown in [25].

Ultra-wideband (UWB) CMOS SoC radar for cardio-pulmonary monitoring has also been implemented [26], but its functionality hasn't been fully proved yet.

### 1.2.4 UWB technology for biomedical applications

Motivated by the same perspective above, we have proposed an innovative system using a specific approach to detect heart and breath rates, which is based on UWB pulse technology [27]. Traditional ECG techniques reported above allow the detection of electrical activity related with heart movements. Unfortunately, in presence of cardiac pathologies, the electrical activity can be unable to reflect the actual mechanical activity of the heart wall. The sensor proposed is directly sensitive to the actual movements of the hearth. Moreover, it can also sense lungs movements related with the expansion and relaxation phases of the respiration. The basic operating principle consists in sending a sequence of extremely short electromagnetic pulses towards the heart and detecting its movement by correlating the echoes reflected from the heart wall with local (i.e. on-chip) replicas of the transmitted pulses properly delayed, as explained in the following section. The frequency spectrum of the transmitted signal results to be very large, whereas the transmitted power is very low as well as required by FCC (Federal Communication Commission) [28] (i.e. lower -41.3 dBm/MHz in 3.1-10.6 GHz), and ETSI (European Telecommunications Standards Institution) [29]. This means that the system can work properly also in an environment where only extremely low level of RF emissions may be tolerated (e.g. in a hospital), but it is also suitable for outdoor environment since it is robust in case of strong RF interfering signals.

The innovation consists in the use of UWB pulse radar technology for sensing heart activity. This allows the realization of a wearable, wireless medical imaging system that does not require any contact with the human body. With respect to the CW Doppler radars, this solution leads to extremely low power consumption. In fact, since the duration of the pulse transmitted is very short (hundreds of picoseconds) compared to the pulse repetition period (in the order of microseconds), then the transceiver can be switched off most of the time (i.e. the circuit is expected to be on approximately for 2 ns every one microsecond, corresponding to 0.2% of the time), leading to extremely low energy consumption (approximately equal to 180 pJ per pulse). Moreover, one of benefits of UWB technology is related also to the opportunity of implementing systems that operate in compliance with international standard regulations.

It is also worth emphasizing that this contact-less sensor uses RF (i.e. wireless) energy for sensing, which is different from the common concept of "wireless sensor", in which a sensor exploits a wireless link with the coordinator node, or another sensor, of the network. In the most common case, the term "wireless" does not reflect the nature of the sensor, which can be with or without any contact with the body. Our sensor makes use of UWB technology to implement contact-less wireless sensing, regardless of the wireless data communication as possible radio link for the sensor node.

## *1.3 UWB radar sensor description*

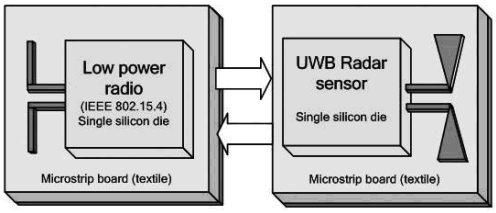


*Fig. 2 – Wearable wireless interface for the heart monitoring: system idea consisting of a fully integrated UWB radar sensor and low-power radio link interface.*

In this context, our wearable contact-less sensor is expected to be a new enabling technology for cardio-pulmonary monitoring. Miniaturization is a key factor to realize such a wearable device, and the latest advances in CMOS technologies allow the realization of highly miniaturized, low-cost and low-power sensor on a single silicon chip of few square millimetres. The radar sensor described herein has been realized in 90nm CMOS technology (ST-Microelectronics). The system consists of a fully integrated UWB radar sensor and a low-power radio interface (see Fig. 2) that will be inserted into an inner garment [27].

### 1.3.1 Operating principle

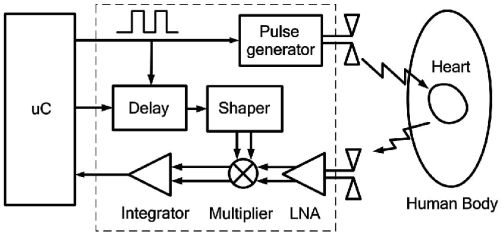


*Fig. 3 – Block diagram of the proposed fully integrated UWB radar for the detection of heart and breath rates. The realized radar sensor is highlighted into the dashed line box.*

The radar sensor adopts a correlation-based topology shown in Fig. 3. The pulse generator transmits a train of extremely short electromagnetic pulses towards the heart wall (the time duration is in the range of 200-400 ps). Since the heart muscle and the blood inside the heart have different characteristic impedances, part of the energy of the transmitted signal is reflected at the surface of separation of these two different media [16]. This energy is detected by the receiver, which consists of a Low Noise Amplifier (LNA), a multiplier and an integrator.

After a time delay approximately equal to the flight time of the pulse, from the transmitter to the receiver (about two nanoseconds), the echoes received from the heart wall are multiplied with a delayed local replica of the transmitted pulses generated by the shaper (see Fig. 3).

Since the time delay is fixed, a fixed range gate is monitored by the radar, and the amplitude of the signal at the output of the multiplier is related to the position of the heart-blood interface. The integrator averages a great number of pulses [30], in order to increase the signal-to-noise ratio at the output. Cardiac and respiratory rates can be read from the slow fluctuations of the output signal (i.e. the heart moves according to its own motion, but it is also influenced by the respiratory activity). Since such vital signs vary at most within a few Hertz, an integrator bandwidth of 100 Hz will be large enough to properly detect them [17]. The feasibility of the radar sensor and the specifications of all radar building blocks have been derived by means of both theoretical model and simulations in large part supported by experimental results [30].

### 1.3.2 Intra-body channel

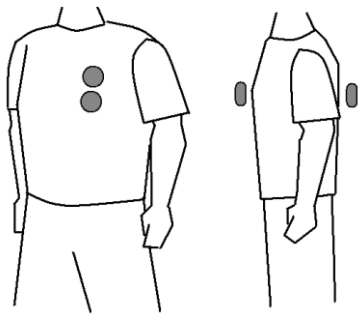


*Fig. 4 – Antennas placement for the intra-body channel-loss measurement: a) same side of the chest and b) front-to-back.*

As for the intra-body channel in which the pulse propagates (i.e. the human chest), a theoretical frequency dependent model has been developed and included into simulations [30]. This model takes into account i) path loss, ii) attenuation in tissues and iii) losses due to reflections at the interface between different tissues. Properties of body tissues have been extracted by parametric models developed by C. Gabriel (et al.) at the Brooks Air Force Base (US.A.) [31, 32]. Simulation results show that the average power loss of the electromagnetic pulse in the 3.1-10.6 GHz band amounts to about 80 dB. The cannel loss model has been confirmed by means of intra-body loss measurements [33], which have been carried out in accordance with the setup reported in Fig. 4. In [34] similar results are achieved.

All building blocks (LNA [35], pulse generator [36], delay generator [37] and multiplier [38]) have been designed and realized successfully as stand-alone circuits first, and then co-integrated in 90nm CMOS technology (ST-Microelectronics) into a single-chip radar sensor that has been tested at Tyndall National Institute.

## *1.4 Textile platform*

The textile platform is the core technology under development in the European project ProeTEX. It aims at developing the technological platform which will allow the monitoring of emergency rescuers, without interfering with their common working activity. To reach this goal the project's consortium has developed a set of smart garments for the acquisition of physiological activity and environment-related parameters [11].

In spite of the approach used in the project (not strictly oriented to implement a full wireless textile platform) this research could be adopted in future extensions toward this kind of application (a WBAN based on a textile platform of autonomous sensors). The current infrastructure allowing remote data communication, information extraction and alarm generation, has been designed and is under development. ProeTEX prototypes address civil protection and fire-fighter requirements, integrating sensors and electronics into the textile platform. However, the results derived by this project can be extended to different bio-monitoring WBAN contexts, as well as health, sport, etc. Prototypes are based on a T-shirt or Inner Garment (IG) and a jacket, or Outer Garment (OG), which are endowed of wearable multipurpose sensors aimed at real-time monitoring relevant parameters, as reported in Fig. 5.

a) b)

*Fig. 5 – Sensor placement on ProeTEX textile platform (a) Inner Garment: 1. Textile Electrodes – Heart Rate monitoring, 2. Piezo-Resistive or Piezo-Electric Sensor – Breathing Rate monitoring, 3. Body Temperature Sensor (b) Outer Garment: 1. Wi-Fi module and Textile Antennas, 2. Wrist & Collar Accelerometers – Activity Assesment, 3. Environmental Temperature Sensor, 4. CO (Carbon Monoxide) Sensor, 5. Visual Alarm Module, 6. Acoustic Alarm Module, 7. Textile Monitor Sensor, 8. GPS receiver, 9. Professional Electronic Box.*

The IG (Fig. 5-a) is dedicated to those physiological measurements that need direct contact or proximity with the skin, while the OG (Fig. 5-b) deals with activity and environmental parameters. A Professional Electronic Box (PEB) is hosted in the OG and it collects the elaborated information from the sensor nodes. The data collected by the PEB are sent in real-time to the Local Coordinator of operations, by means of a Remote Transmission System working with Wi-Fi protocol. A Monitoring Software, running on the local coordination workstation, visualizes in real-time the information extracted from the data and automatically activates alarms when dangerous contexts are detected. By using a long range communication system, relevant information can be sent from Local Coordinators posts to Central Emergency Coordinators.

### 1.4.1 Inner garment

The IG (Fig. 5-a) prototype is based on a T-shirt having two main areas devoted to specific tasks: (1) an elastic region including all textile sensors and (2) a region containing a detachable on-board electronics. The project plans the use of textile sensors and electrodes, connected to electronic modules through textile conductive cables integrated in the shirt. The detachable board acquires and processes the IG

sensors signals and transmits the elaborated information to the PEB through a RS485 bus. In particular the HR is obtained by means of two textile electrodes, realized as described in [39]. The breathing rate (BR) sensor is realized by means of textile deformation sensors detecting the local fabric deformations due to chest movements during respiration employing a piezoelectric transducers in wire form, integrated in the IG [40]. The body temperature (BT) measurement is carried out by using a digital sensor embedded in the shirt in a proper pocket at the left armpit level described in [41]. Such a support lends itself to a future wireless use, allowing the placement of a new generation of wearable sensors as part of a WBAN.

### 1.4.2 Outer garment

The OG (Fig. 5-b) includes the subsystems for assessing the operator activity state and monitoring the surrounding environment. Positions and aims of sensors are highlighted in Fig. 5 [42, 43]. All OGs incorporate a Long Range transmission module equipped with commercial Lithium Ion-Polymer battery, which gives power supply to the garment electronics, allowing autonomy up to seven hours. Within the current ProeTEX concept the processing logic is distributed at the sensor level. Each measurement node is implemented through a dedicated sensor module that contains the sensor itself, the analog frontend and a low power microcontroller which operates AID conversion, signal processing and information extraction. The IG and OG modules send the elaborated information to the PEB through the RS485 bus (four wires, two for data and two for power supply, i.e. industrial standard for sensors networks). Within the future perspective of extending the results of this project to bio-monitoring WBAN, these communications between sensor nodes and PEB (i.e. the Personal Server) will be completely wireless and the sensor will be almost invisible to the patient thanks to their reduced size and textile support.

## *1.5 Processing and networking*

In addition to hardware specifications, such as minimal weight and miniaturized size, low power consumption for prolonged continuous monitoring, sensor design has to take into consideration the need of integration in WBANs, which is related to processing and networking, including standard based interface protocols, patient-specific calibration, tuning and customization. From this point of view, it is useful to distinguish the sensor itself, as the transducer from physical to electric signals, and the sensor node that continuously acquires, converts and elaborates the sensor signals, and transmits them wireless to the Personal Server. This modular architecture allows the reduction of both the overall hardware complexity and amount of data to be sent, which emphasizes how hardware resources and power consumption are strongly related. Whenever possible, one of the best effort in processing and networking has to be done in the direction of implementing local processing at the minimum cost in terms of hardware and power consumption resources, so that limiting data transmission by means of the radio link. The application of this basic concept has led to sensor nodes capable of implementing data filtering and distributed processing, contributing in considerably reducing the power consumption required by the radio link [44].

### 1.5.1 Sensor node

Therefore, the strategy to implement the sensor node has a fundamental role in the efficiency of the WBAN. As for the processing, some works based on ECG signals suggest interesting solutions [45]. However, since our system is not supposed to extract an ECG signal, a different analog signal processing is needed in our case. The fundamental building blocks will be an amplifier, an analog-to-digital converter (ADC), a digital signal processor (DSP) and a RF transmitter. As for the sensor node, it is expected to have extremely reduced size, as well as for the sensor itself. Low-power and low-voltage design techniques have to be extensively implemented in order to minimize power consumption. In [45] a fully-integrated SoC sensor node adopting these methods is reported. The feasibility of such a system with wearable and wireless features is demonstrated. Simulations show that signal amplitude of some millivolts is expected at our sensor outputs [38] and this is the kind of signal that the amplifier (i.e., first block of the sensor node) has to be able to detect. In [13] a system capable of processing signals with peak-to-peak amplitude as low as 5 mV, is presented. This sensor node is designed to process ECG signals, but it is also proven to be capable of processing signals detected by a Doppler radar sensor. These processing techniques are similar to those useful for the output signals of our sensor, even if the system itself is based on a different principle of operation. In regard of the DSP and RF transmitter units, their characteristics will depend on the radio link technology chosen to realize the data communication with the Personal Server.

### 1.5.2 Communication standards

In [3] the most promising solutions for WBAN networking are listed. Some recent works on WBANs employ ZigBee standard, as in our system [27]. At the current stage, this provides one of the best perspectives for WPAN connectivity. However, in the case of WBAN for bio-monitoring and health assistance, new emerging standard (e.g., IEEE 802.15.6) will possibly employ UWB. In principle, this will permit the implementation of efficient wireless link with higher data rate, lower power consumption and system complexity with respect to narrowband counterparts. The future development of this standard is not clear at this stage, i.e. it will depend on the commercial consensus. Moreover, some additional technical complexity of time-domain radio link technology seems to suggest a moderate level of confidence in UWB data link at this stage. It is worth pointing out that heart movement produces low frequency signals, which rarely need high data rate radio link, therefore a narrowband radio link could be preferred anyway, especially considering the possible evolution of IEEE 802.15.4a standard [46]. In this frame, Bluetooth Low Energy Technology (LEE) could be another good candidate [46]. Low power consumption is always one of the main goals of communication standards. LEE is expected to allow the complete compatibility with the well established Bluetooth standard, while sensibly reducing power consumption without affecting data-rate. In this way every commercially available Bluetooth compatible device (e.g., Smart Phone) can operate as Personal Server of our WBAN. This aspect could represent probably the most relevant factor for the development of such radio link technology. As long as the connection with the Personal Server is established, a WBAN can easily widen to different levels, from personal to metropolitan and worldwide networks. Different levels of hierarchy permit different applications to coexist. In the specific area of the health care these

networks will allow low-cost, non-invasive, continuous, ambulatory health monitoring with quasi real-time updates of medical records via net.

## *1.6 Summary*

An overview of the state of the art in health care assistance has been reported, with special focus on identifying some open challenges and innovative solutions in heart health assistance. Some of the preliminary results and future perspectives of the on-going research projects have been summarized, with special emphasis on the European project ProeTEX. This is aimed at implementing a wearable sensor platform for bio-monitoring. In the same framework, the research aimed at implementing a new class of sensors for contact-less cardio-pulmonary monitoring based on system-on-chip pulse radar is reported.

Moreover, the opportunity of merging contact-less sensor into a wearable textile platform is discussed. It will offer the interesting perspective of delivering an innovative enabling technology for advanced heart health wireless assistance, in response to the increasing needs of large scale and accessible medical service for monitoring the cardio-pulmonary chronic diseases of the population.

WBAN can be the answer to the high demand of innovation in health care assistance. For this reason an important aspect is the design of sensor nodes, considering processing and networking in accordance with the perspectives reported above.

# 2. UWB MULTIPLIER: DESIGN AND EXPERIMENTAL RESULTS

## *2.1 Introduction*

The challenges regarding the wide band requirements introduced by UWB applications have contributed to revolutionize the RF design conception of circuits and systems [47-49] and also led to a reconsideration of time domain techniques for the experimental verifications. The radar that has been developed by the research group is based on a correlation receiver topology. One of the fundamental building blocks of the receiver is the wide-band multiplier. This circuit, with the subsequent integrator, realizes the correlation between the local replicas of the pulses transmitted and echoes received. In order to accomplish the radar system requirements, dominated by high linearity, wide band and low power consumption, an analog wide-band multiplier based on a specific circuit arrangement around the Gilbert's quad multiplier cell has been designed and tested and is presented in this chapter.

The material presented in this chapter is reported in [50].

## *2.2 Wide-band multiplier design*

The design of wide-band multipliers and mixers for UWB applications has recently generated a large interest in the RFIC community [51-54]. Most of the solutions are based on the evergreen Gilbert multiplier and commonly implemented by means of n-MOSFET transconductance and multiplier stages. In some case related with mixer design, the transconductance stage is replaced by a common-gate stage [55], which is affected by poor noise performance.

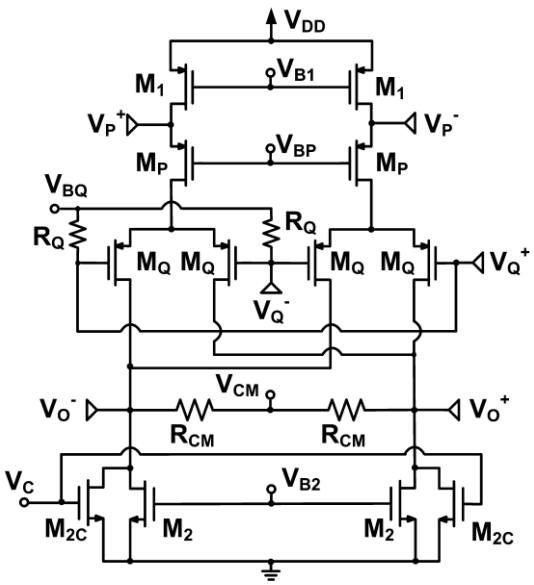


*Fig. 6 – Schematic of the multiplier (core). $V_{BP}$, $V_{BQ}$, $V_{B1}$, $V_{B2}$ are dc voltages obtained by internal references of Fig. 7-a. $V_C$ and $V_{CM}$ are related with the CMFB circuit of Fig. 7-b.*

Although from a topological point of view multiplier and mixer are similar, their designs differ essentially because of the different approach to the quad cell. A mixer is typically designed and optimized according to frequency domain metrics as the conversion gain, whereas a multiplier is better investigated using time domain analysis. This is even truer for UWB devices, which work with pulses.

In response to the specific requirements of the emerging UWB pulse radar applications, a specific circuit arrangement around the Gilbert's multiplier cell aimed at obtaining

adequate band and linearity with low power consumption is proposed herein. The multiplier circuit is reported in Fig. 6.

In order to accomplish the wideband requirements, the proposed multiplier exploits a p-MOSFET common-gate differential pair input stage (transistors $M_P$), which allows us to implement a low-complexity input impedance matching to the low noise amplifier (LNA) output impedance over a wide band. In fact, the input capacitance (i.e. mostly drain-to-bulk capacitance of $M_1$) of the multiplier can be compensated by the output-stage peaked inductors of the UWB LNA [35]. It is worth mentioning that the common-gate input stage has been exploited to achieve wideband input impedance matching in the UWB LNA but not yet for the design of multiplier for UWB applications. In this way, an effective inter-stage impedance matching between LNA and multiplier is obtained avoiding significant bandwidth degradation. This is an important design aspect, quite often neglected, that on the contrary, has to be considered when looking for wideband gain performance. The multiplier stage consists of a p-MOSFET Gilbert's quad (transistors $M_Q$).

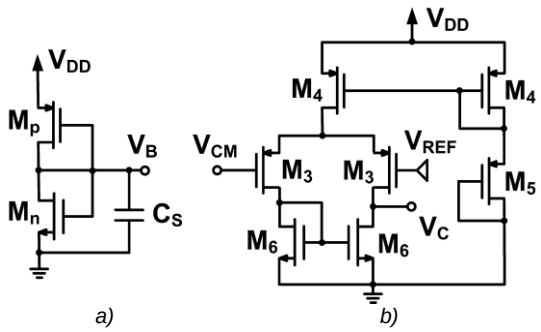


*Fig. 7 – Voltage reference circuits. a) Schematic of the generic circuit adopted to generate each of the four different internal voltages $V_{BP}$, $V_{BQ}$, $V_{B1}$ and $V_{B2}$ (i.e. the subscript "x" is for P, Q, 1 and 2). $C_S$ is a shunt capacitor. b) CMFB circuit. $V_{REF}$ is an external dc voltage reference.*

The circuit includes the transistors $M_1$ at the input and $M_2$ at the output, which have been implemented with non-minimum channel length in order to increase their output resistance and then reduce the signal losses in the circuit. The internal dc voltage references are provided by four different circuits as in Fig. 7-a, whereas the common mode (CM) voltage at the output node is regulated by the CM feed-back (CMFB) circuit through $V_{CM}$ and $V_C$ (Fig. 7-b).

### 2.2.1 Multiplier linearity

High linearity range and low power consumption are contradictory requirements (i.e. typically increasing the linearity range corresponds to increase the power consumption). In order to alleviate the linearity performance degradation due to low current consumption, both multiplier and common-gate differential pair stages have been implemented by using p-MOSFETs. Associated with a lower gain, this choice allows us to achieve approximately the same input linearity range of peer-size n-MOSFETs with the same overdrive voltage, but with a lower current consumption.

Therefore, relying on input differential pair and multiplier stage, both implemented with p-MOSFETs, in principle it is possible to achieve adequate band and linearity performance without the need to increase the bias current.

### 2.2.2 Multiplier core design

Considering the short channel approximation (1), (2) in [57], the current in a MOSFET can be written as in (3). This will help following some of the following passages.

$$I_d = \mu \frac{C_{ox}}{2} W \left(V_{gs} - V_t\right) E_{sat} \tag{1}$$

$$g_m = \mu \frac{C_{ox}}{2} W E_{sat} \tag{2}$$

$$I_D = g_m \left(V_{sg} - V_{th}\right) \tag{3}$$

Let's consider the circuit in Fig. 8 to analytically analyze the multiplier. The output can be expressed as follows:

$$V_O = \left(I_{L^+} - I_{L^-}\right) \cdot Z_L = \left[\left(I_{Q4} + I_{Q2}\right) - \left(I_{Q1} + I_{Q3}\right)\right] \cdot Z_L$$

$$V_O = \left[\left(I_{Q4} - I_{Q3}\right) - \left(I_{Q1} - I_{Q2}\right)\right] \cdot Z_L \tag{4}$$

where $Z_L$ is the output load.

Using (3) the current differences in each side of the quad can be expressed in (5) and (6) and derived as follows:

$$I_{Q4} - I_{Q3} = g_{mQ4}\left(V_{sgQ4} - V_{th}\right) - g_{mQ3}\left(V_{sgQ3} - V_{th}\right)$$

$$I_{Q4} - I_{Q3} = g_{mQ3,4}\left(V_{sgQ4} - V_{th} - V_{sgQ3} + V_{th}\right)$$

$$I_{Q4} - I_{Q3} = g_{mQ3,4}\left(V_{sQ4} - V_{gQ4} - V_{sQ3} + V_{gQ3}\right)$$

$$I_{Q4} - I_{Q3} = g_{mQ3,4}\left(V_{gQ3} - V_{gQ4}\right)$$

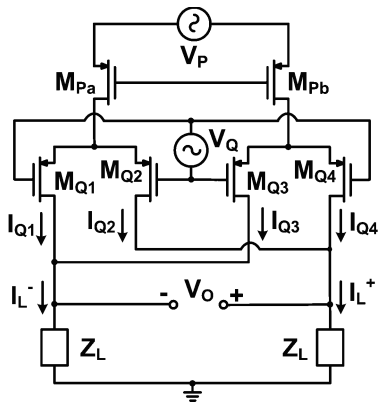


*Fig. 8 – Multiplier schematic for analytical analysis.*

$$I_{Q4} - I_{Q3} = g_{mQ3,4} V_Q \tag{5}$$

$$I_{Q1} - I_{Q2} = g_{mQ1,2} V_Q \tag{6}$$

This can be obtained under the hypothesis that Gilbert Cell transistors $M_{Q1}$-$M_{Q2}$ and $M_{Q3}$-$M_{Q4}$ have, respectively, the same transconductance $g_m$ and the same threshold voltage $V_{th}$.

$V_O$ can now be expressed as in (7):

$$V_O = \left(g_{mQ3,4} - g_{mQ1,2}\right) Z_L V_Q \tag{7}$$

Again considering (3) the transconductance can be expressed as in (8) and (9):

$$g_{mQ1,2} = \frac{I_{Q1,2}}{\left(V_{sg} - V_{th}\right)_Q} = \frac{I_{Pa}}{2\left(V_{sg} - V_{th}\right)_Q} = \frac{g_{mPa}\left(V_{sgPa} - V_{th}\right)}{2\left(V_{sg} - V_{th}\right)_Q} \tag{8}$$

$$g_{mQ3,4} = \frac{I_{Q3,4}}{\left(V_{sg} - V_{th}\right)_Q} = \frac{I_{Pb}}{2\left(V_{sg} - V_{th}\right)_Q} = \frac{g_{mPb}\left(V_{sgPb} - V_{th}\right)}{2\left(V_{sg} - V_{th}\right)_Q} \tag{9}$$

The output voltage can be then expressed as in (10) and derived as follows:

$$V_O = \left(g_{mQ3,4} - g_{mQ1,2}\right) Z_L V_Q$$

$$V_O = \left( \frac{g_{mPa}\left(V_{sgPa} - V_{th}\right)}{2\left(V_{sg} - V_{th}\right)_Q} - \frac{g_{mPa}\left(V_{sgPa} - V_{th}\right)}{2\left(V_{sg} - V_{th}\right)_Q} \right) Z_L V_Q$$

$$V_O = \frac{g_{mP}\left(V_{gPa} - V_{gPb}\right)}{2\left(V_{sg} - V_t\right)_Q} Z_L V_Q$$

$$V_O = \frac{g_{mP} V_P}{2\left(V_{sg} - V_{th}\right)_Q} Z_L V_Q \tag{10}$$

In a low-frequency approximation, applying (3) once again, the output voltage ($V_O$) of the multiplier is expressed by (11), where $Z_L$ is the output load, $V_P$ and $V_Q$ are the two input voltages and $I_{DQ}$ the dc drain current of $M_Q$.

$$V_O = \frac{1}{2} g_{mP} \frac{g_{mQ}}{I_{DQ}} Z_L V_P V_Q \tag{11}$$

Therefore, since $g_{mP}$ is sized in order to accomplish the input impedance matching, maximizing the gain leads to a maximization of the transconductance to drain current ratio $g_{mQ}/I_{DQ}$. In deep sub-micron MOSFETs the carrier velocity saturates and the transconductance increases almost linearly as the dc drain current ($I_D$) increases. Therefore, a trade-off between gain and dc power consumption ($P_C$) is required for an effective design. By investigating the characteristics of the p-MOSFETs, it can be observed that $g_m/I_D$, which is an invariant of the technology node, exhibits a knee as in Fig. 9.

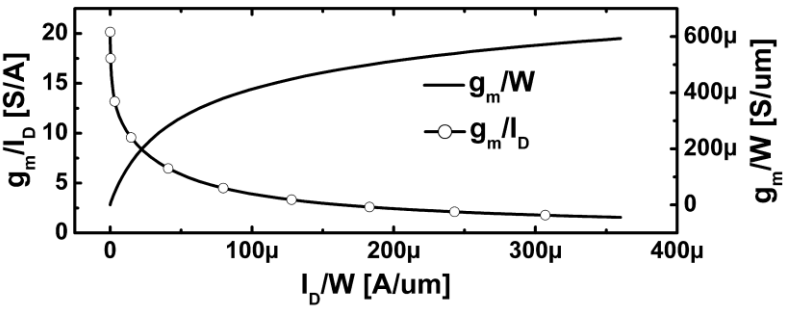


*Fig. 9 – $g_m/W$ and $g_m/I_D$ of the p-MOSFET versus the drain current density per gate width ($I_D/W$).*

The region on the left of the knee is characterized by moderate $g_m$ for low current consumption. Therefore, this region can be exploited to identify the current density for a convenient gain- to-current ratio for the p-MOSFET of the quad ($M_Q$). Once $g_{mQ}/I_{DQ}$ has been chosen, $I_{DP}$ is given since $I_{DP} = 2\, I_{DQ}$. Therefore, by considering the input equivalent resistance ($1/g_{mP}$) in the low-frequency approximation, $M_P$ and $M_Q$ can be sized in order to accomplish simultaneously the requirements in terms of impedance matching (200Ω-diff, i.e. the LNA output impedance) and trade-off gain-power. Moreover, the input-output energy ratio introduced hereinafter allows us to maximize the performance by means of a fine tuning of the area size of $M_P$ and $M_Q$. To avoid signal losses through low impedance paths, input and output active loads (transistors $M_1$ and $M_2/M_{2C}$, respectively) are implemented.

#### *2.2.2.1 Frequency domain metric: Conversion gain*

The multiplier has to be tested in order to verify its readiness to a single pulse. In UWB applications the correlation occurs between pulses of the same shape at the same frequency, so it would be useful to test the multiplier direct conversion capability instead of considering a non-zero IF. Unfortunately measurement results can only be obtained for a non-zero IF.

In order to evaluate the circuit performance, the literature reports the conversion gain ($G_C$), also expressed in terms of voltage, as follows,

$$G_C = \frac{P_{IF}}{P_{ARF}}, \qquad G_{CV} = \frac{V_{IFM}}{V_{RFM}} \tag{12}$$

where $P_{IF}$ is the output power at the intermediate frequency (IF) and $P_{ARF}$ is the input power available at the RF input; $V_{IFM}$ and $V_{RFM}$ are the correspondent maximum voltages.

$G_C$ is conceived for mixers, in which the quad behaves as a switching stage, and the main advantage is that it allows the use of tones as test signals rather than ad-hoc shaped pulses.

#### *2.2.2.2 Time domain metric: Input Output Energy Ratio*

In case of short pulses (wide-band), the test tones and the frequency domain analysis are not close to the operating conditions, therefore a design optimization by using a time domain analysis is desirable to maximize the output voltage corresponding to maximum correlation between two input pulses. For these reasons, we introduce herein the Input-Output Energy Ratio (IOER) as a time-domain metric defined as follows,

$$IOER = \frac{\int_{t_{o1}}^{t_{o2}} v_o^2(t)\,dt}{\int_{t_{i1}}^{t_{i2}} v_i^2(t)\,dt} \tag{13}$$

where $t_{o1}$ and $t_{o2}$ are the start time and stop time of the output pulse, respectively, whereas $t_{i1}$ and $t_{i2}$ are the corresponding values for the input pulse.

Despite the IOER may be defined for both inputs, in our case we considered only input P since this is related to the received echo (i.e. relatively small signal amplified by the LNA), rather than the local replica (i.e. robust signal generated on-chip).

The multiplier core has been designed considering the criteria above, achieving a good trade-off between $G_C$, noise figure (NF), impedance matching and power consumption ($P_C$). The transistors sizes are reported in Table I (Part 1).

TABLE I: TRANSISTORS SIZING

| | | | | | |
|---|---|---|---|---|---|
| Part 1 | | $M_1$ | $M_P$ | $M_Q$ | $M_2$ |
| | W/L | 16/0.2 | 40/0.1 | 40/0.1 | 10/1 |
| Part 2 | | x=1 | x=P | x=Q | x=2 |
| | Wp/Wn, L | 36/5, 0.5 | 25/13, 0.7 | 9/11, 0.7 | 23/14, 0.7 |
| Part 3 | | $M_3$ | $M_4$ | $M_5$ | $M_6$ |
| | W/L | 6/0.1 | 120/1 | 120/1 | 10/1 |

### 2.2.3 Bias circuits design

The dc voltages $V_{BP}$, $V_{BQ}$, $V_{B1}$ and $V_{B2}$ are generated internally by means of four different circuits as that in Fig. 7-a; they are equal to 550, 470, 680 and 530 mV, respectively.

The biasing circuit is regulated by the following equation:

$$I = K_n^{'}\left(\frac{W_n}{L_n}\right)\sqrt{\left(V_B - V_{th_n}\right)} = K_p^{'}\left(\frac{W_p}{L_p}\right)\sqrt{\left(V_B - V_{th_p}\right)} \tag{14}$$

As regards the sizing let's consider the following equations:

$$\frac{W_p}{L_p} = P \tag{15}$$

$$\frac{W_n}{L_n} = N \tag{16}$$

$$P = cN \tag{17}$$

where c is a variable.

$L_p$ and $L_n$ are fixed to a convenient value (0.5 μm). By choosing N, the current I on the MOSFETs can be fixed as equal to the current in the MOSFET that has to be biased. By choosing c, $V_B$ can be fixed to the desired value. In order to reduce the $P_C$ and achieve adequate design reliability, the MOSFETs have been sized as in Table I, Part 2. The Monte Carlo analyses on the multiplier without CMFB circuit show a weakness on the input and output voltages reliability. In spite of the robustness of the dc voltage references generated on chip, the input and output voltages exhibit high variability with process variations. This variability is due to the specific topology where inputs and output are stacked on a single stage of four transistors under a 1.2-V voltage supply. Specifically, at the output nodes two drains, one of a p-MOSFET and one of an n-MOSFET, face each other. In this condition, the strong signal on the quad input can easily put the output dc voltages out of balance. For this reason a CMFB circuit has been specifically designed to control the voltages at those nodes.

The CMFB circuit is based on the design principle in [58]. This circuit senses the CM voltage $V_{CM}$ of the multiplier core using resistive divider ($R_{CM}$) as CM detector circuit. The CM voltage $V_{CM}$ is compared to the external reference voltage $V_{REF}$ in the differential pair ($M_3$). The CMFB circuit output is the voltage $V_C$ which controls the current drained by $M_{2C}$ in order to maintain the dc output voltage close to $V_{REF}$ (0.6 V). The aspect ratios are reported in Table I, Part 3. The frequency response (magnitude and phase) of the CMFB network is reported in Fig. 10.

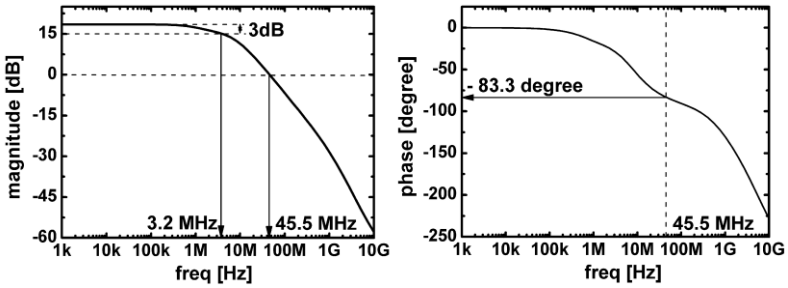


*Fig. 10 – Frequency response {$V_C(f)/V_{CM}(f)$} of the CMFB network: a) magnitude and b) phase. The ac signal is applied to the $V_{CM}$ node as an independent input, whereas the output signal is collected at the $V_C$ node while connected to the multiplier core circuit.*

Note that the phase margin is about 83°, which is reasonably large to prevent any stability problem. The results of the Monte Carlo analyses reported in Fig. 11a-g show the good robustness of the dc voltage references generated on-chip, the dc voltages at the input P and the output of the multiplier, and the overall dc current ($I_{DD}$) drained from the supply voltage ($V_{DD}$).

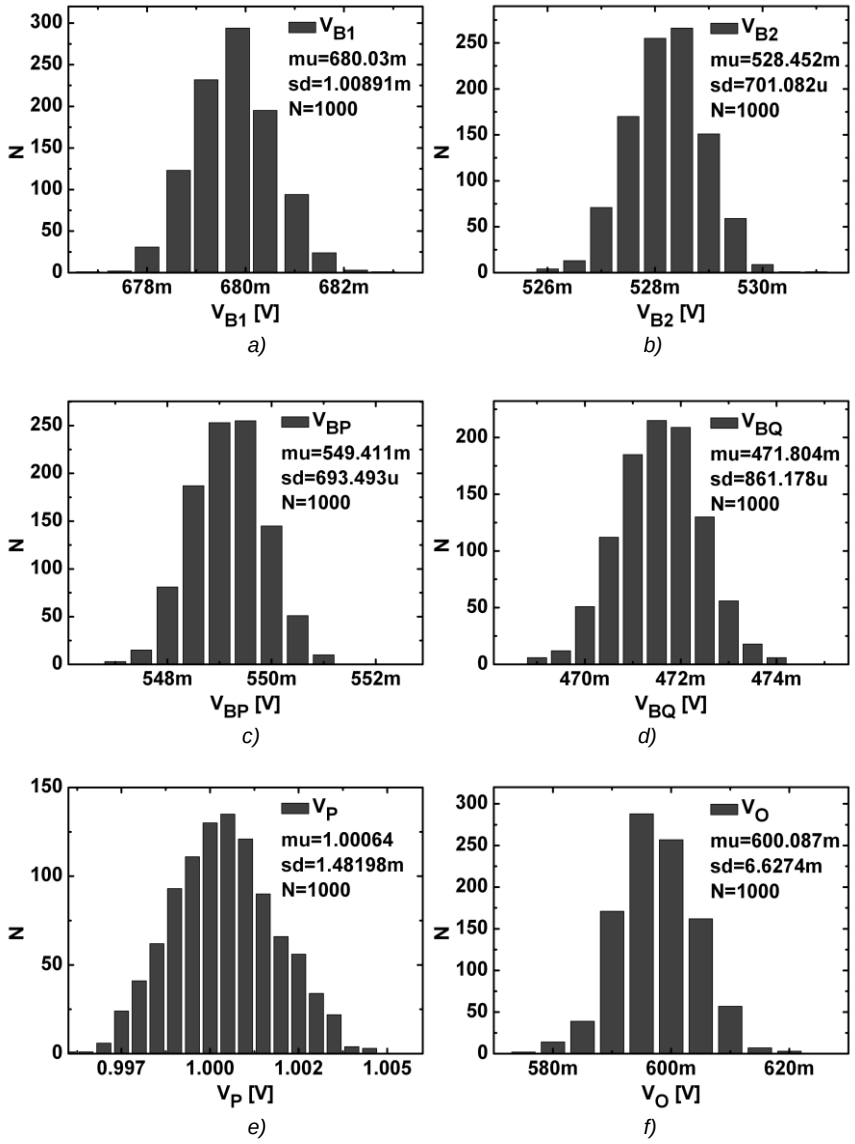

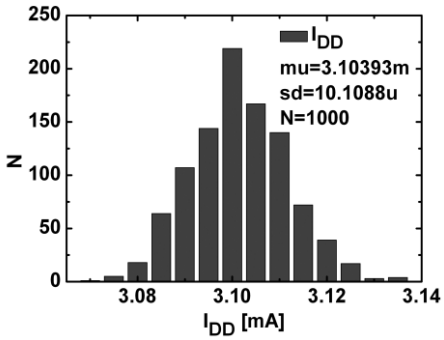


*g)*

*Fig. 11 – Results of the Monte Carlo analyses (1000 iterations) for process and mismatches variations: a) $V_{B1}$, b) $V_{B2}$, c) $V_{BP}$, and d) $V_{BQ}$. dc voltages at the e) input P and f) output. g) Overall dc current ($I_{DD}$) drained by the supply voltage ($V_{DD}$).*

### 2.2.4 Simulation results

$V_O$ obtained by post-layout simulations (PLS) is reported in Fig. 12, for which the IOER amounts to 3.3.

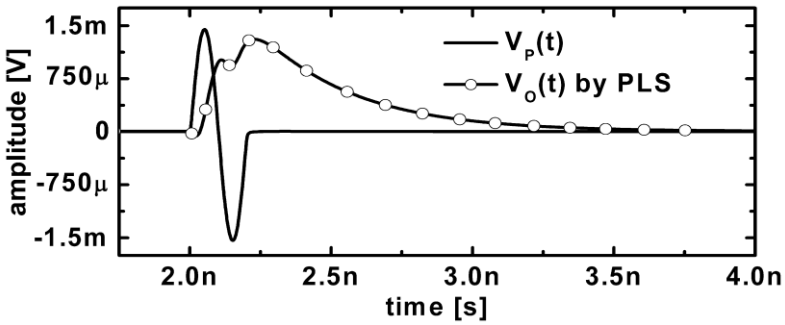


*Fig. 12 – $V_O(t)$ obtained by PLS for time-aligned $V_P$ and $V_Q$ inputs. $V_Q(t)$, not reported for reasons of scale, has the same shape and duration time of $V_P(t)$ (i.e. sinusoidal monocycle pulse) and an amplitude equal to 800 mVpp.*

As mentioned before, the multiplier's $G_{CV}$ should be tested at a zero IF ($G_{CV0}$) as if the circuit was working in the receiver chain followed by the integrator. Since it is not possible to obtain such a measured results, $G_{CV}$ has been simulated both for a zero IF and for an IF= 1 kHz so that the results could be compared to the measured one.

$G_{CV0}$ has been simulated by feeding the multiplier with two synchronous tones ($P_{ARF}$= -15 dBm, $P_{ALO}$= -5 dBm), for sixteen different frequencies all over the 3.1-10.6 GHz band, considering a capacitive load that simulates the presence of the integrator (C~75 fF). Results are reported in Fig. 13. The resulting $G_{CV0}$ is almost 4 around 5 GHz.

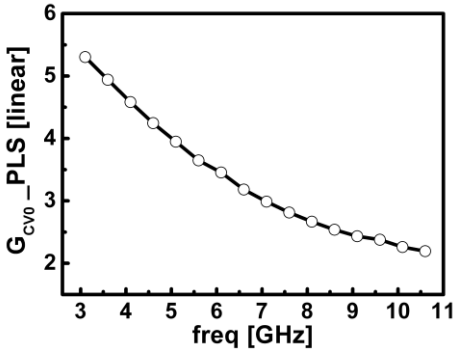


*Fig. 13 – $G_{CV0}$ value over the whole 3.1-10.6 GHz bandwidth.*

$G_{CV}$ has been simulated at IF= 1 kHz with $P_{ARF}$= -15 dBm and $P_{ALO}$= -5 dBm, obtained by considering a load impedance of 50 KΩ || 0.27 pF (i.e. input impedance of the test probe).

NF has been simulated for RF from 3 to 4.9 GHz and LO frequency equal to 5 GHz. This is obtained on standard 50Ω impedance. $G_{CV}$ and NF by PLS are reported in Fig. 14.

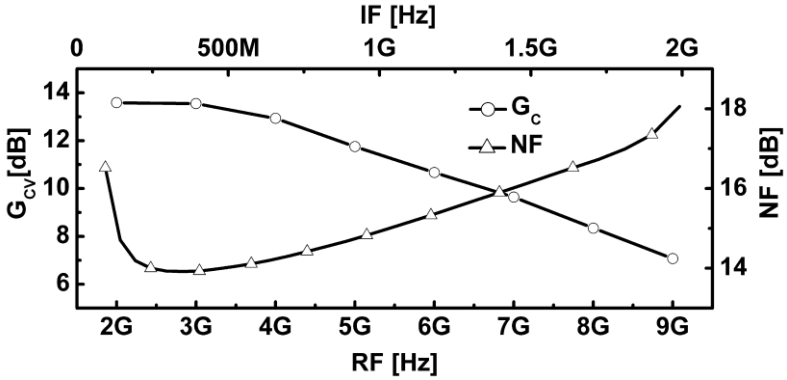


*Fig. 14 – $G_{CV}$ versus RF at IF=1 kHz. NF versus IF (LO-RF) for RF from 3 to 4.9 GHz and LO frequency equal to 5 GHz.*

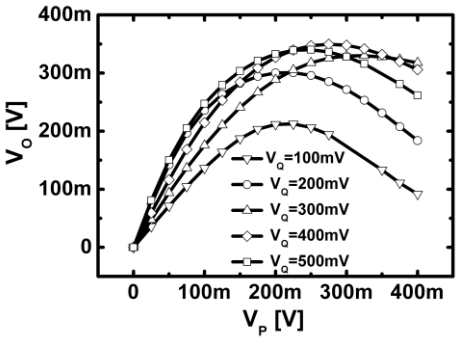


*Fig. 15 – Linear behavior of the multiplier. Those indicated are peak values.*

In order to test the linearity of the circuit, two sinusoidal input signals at the same frequency of 5 GHz have been applied to the P and Q ports. $V_P$(t) peak amplitude value has been swept from 0 to 400 mV while $V_Q$(t) peak amplitude value has been swept from 0 to 500 mV with a step size of 100 mV. The results are shown in Fig. 15.

The $P_{1dB}$ at the input P is −3.47 dBm when $V_Q$(t) peak amplitude value is 500 mV.

## 2.3 Experimental results

The multiplier has been fabricated in 90nm CMOS by STMicroelectronics. The test-chip micrograph is reported in Fig. 16. The circuit operates under a 1.2-V voltage supply and requires an external reference dc voltage ($V_{REF}$) of 0.6 V for the CMFB circuit. The overall $P_C$ is 3.7 mW (0.9 mW for the multiplier core and 2.8 mW for the bias circuits).

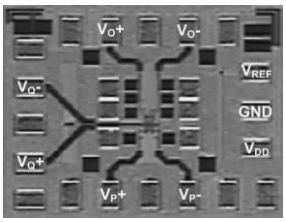


*Fig. 16 – Micrograph of the test-chip. The total area is 560×700 um$^2$ (ESD-protected pads inclusive), whereas the circuit area is 150×200 um$^2$.*

### 2.3.1 Time domain measurements

The multiplier's time-domain performance has been measured by applying two sequences of pseudo-Gaussian monocycle pulse with amplitude of 170 mVpp ($V_P$) and 650 mVpp ($V_Q$), and duration time of 700 ps. $V_O$ has been captured by means of a high impedance (HiZ) differential probe (1134A, with input impedance of 50 KΩ || 0.27 pF) and a digital signal oscilloscope (DSO 54855A) by Agilent. Some pictures of the time domain test setup are shown in Fig. 17.

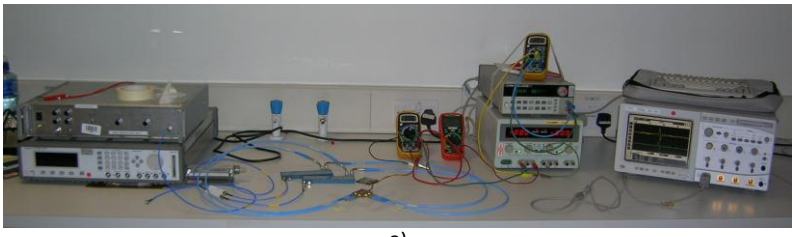

*a)*

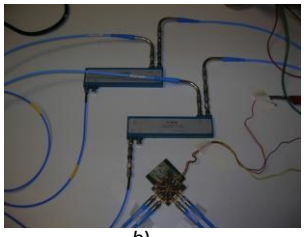

*b)*

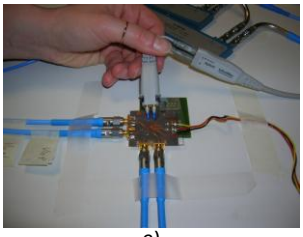

*c)*

*Fig. 17 – Pictures of the time domain test setup. a) Whole test bench with pulse generator on the left, power supplies in the middle and oscilloscope on the right. b) Details of the baluns and test board. c) Details of the test board: RF cables on the inputs and HiZ probing on the output.*

A scheme of the time domain test setup is shown in Fig. 18 where all the details are highlighted.

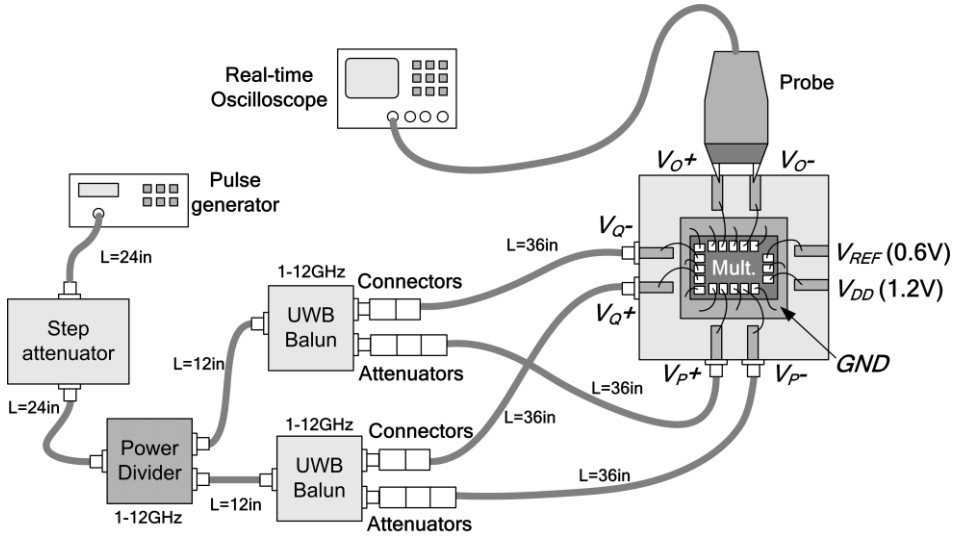


*Fig. 18 – Test setup for the time-domain characterization.*

The pulse generator (i.e. the instrument) could provide only a single ended pulse. The system requires two differential pulses with different amplitudes and with a controllable relative displacement to test the correlation capability. For this reason a power divider and two baluns have been used so that four different pulses could be obtained to be recombined as needed. The Q-input signals' amplitude has been controlled with a step attenuator after the pulse generator. To control the P-input signals' amplitude, that is supposed to be much lower, different set of attenuators have been used on the positive and negative sides of the two different baluns. The other sides were used for the Q-inputs where some additional SMA connectors have been inserted to obtain the different relative delays.

The output signals measured for three different delays between the two input pulses $V_P$ and $V_Q$ are reported in Fig. 19.

Note that when both inputs are time aligned, case (a), the output signal is maximum (i.e. $V_P$ and $V_Q$ are fully correlated), whereas when their relative delay is approximately equal to their duration time (700 ps), case (c), the output signal is zero (i.e. $V_P$ and $V_Q$ are fully uncorrelated). An intermediate condition is reported as case (b). In case (a), the IOER amounts approximately to two.

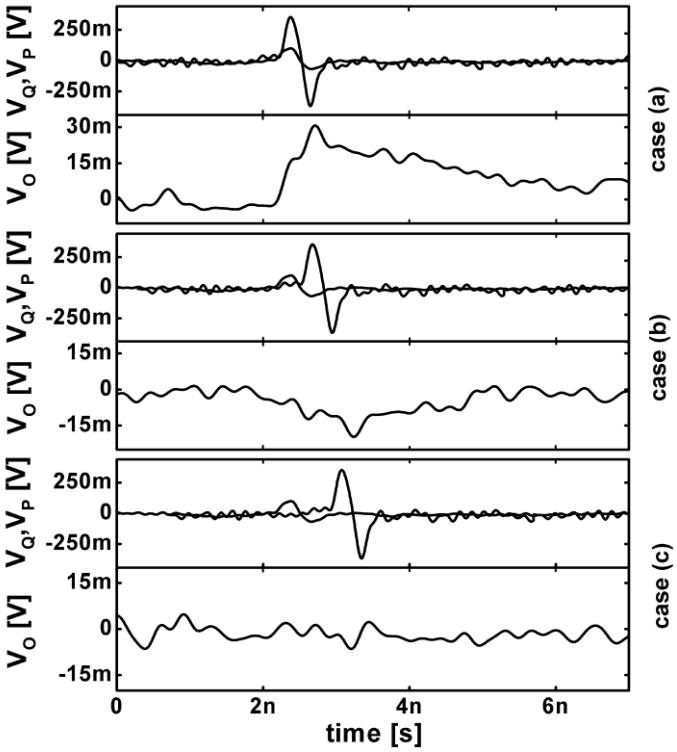


*Fig. 19 – I/O signals measured in three cases: the input monocycle pulses have (a) no relative shift (i.e. time alignment), (b) relative shift of half duration time, and (c) relative shift equal to the duration time.*

### 2.3.2 Frequency domain measurements

In accordance with the common practice in literature and in order to facilitate the comparison with other state-of-the-art (SoA) solutions, the multiplier has been tested also as a mixer. The RF tone has been applied to the differential pair input ($V_P$), whereas the LO to the quad input ($V_Q$), so that an intermediate frequency (IF=RF-LO, i.e. low-side injection) has been measured at the output ($V_O$).

#### *2.3.2.1 Conversion gain*

For this test two signal generators (up to 10 GHz) have been used to obtain the input signals, together with two UWB baluns. $V_O$ has been again captured by means of a high impedance (HiZ) differential probe (1134A, with input impedance of 50 KΩ || 0.27 pF) and a digital signal oscilloscope (DSO 54855A) by Agilent. Some pictures of the frequency domain test setup used to measure the conversion gain of the multiplier are shown in Fig. 20.

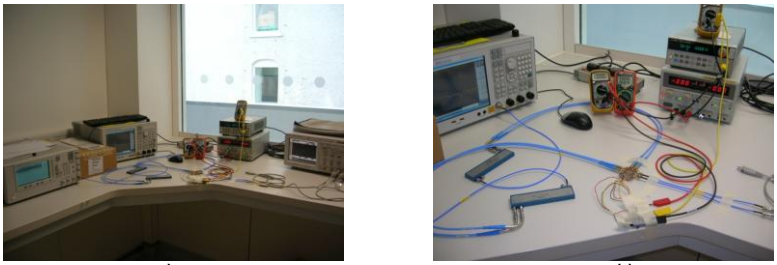

a) b)

*Fig. 20 – Pictures of the $G_{CV}$ test setup. a) Whole test bench with, starting from the left: signal generator, vector network analyzer used as signal generator, power supplies and oscilloscope on the right. b) Details of the baluns, power supplies and test board.*

The measurements for input tones in the range from 2 to 9 GHz for different IF are reported in Fig. 21. Note that $G_{CV}$ is about 12.7 dB for RF in the range from 2 to 4 GHz.

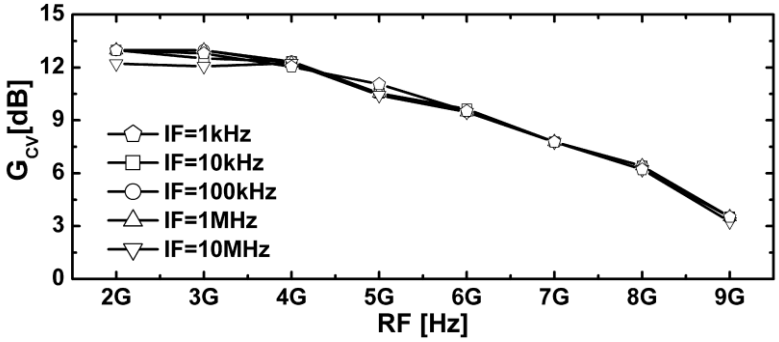


*Fig. 21 – $G_{CV}$ versus RF input frequency, for different IF ($P_{ARF}$= -15 dBm, $P_{ALO}$= -5 dBm). The 3-dB band ($B_{3dB}$) is 0-5.6 GHz.*

#### *2.3.2.2 Linearity*

The test setup for this measurement has been the same as for the conversion gain. Two signal generators have been used to provide the input signals and the output has been capture by HiZ impedance probe and oscilloscope.

The input 1-dB compression point ($P_{1dB}$) amounts to −3.5 dBm ($P_{ALO}$= −5 dBm) and −2 dBm ($P_{ARF}$= −15 dBm) for P and Q inputs, respectively (RF= 3 GHz, IF= 10 MHz, i.e. max gain conditions), as reported in Fig. 22. Similar performance has been measured for four test-chips.

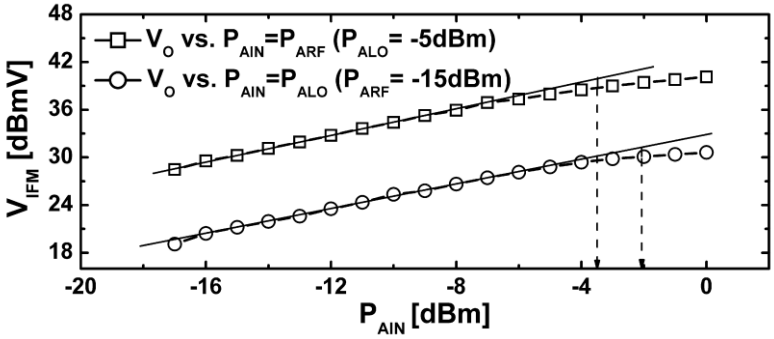


*Fig. 22 – Measured $P_{1dB}$ for P and Q inputs.*

### *2.3.2.3 Noise figure*

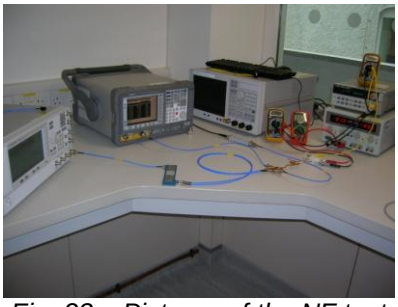

*Fig. 23 – Pictures of the NF test setup. Starting from the left: signal generator, spectrum analyzer used as noise figure meter and power supplies on the right.*

For this test a signal generator has been used to feed the Q-input (LO-port). P-input has been obtained from the noise source powered by the spectrum analyzer E4407 by Agilent that can be used as a noise figure meter. $V_O$ has been captured by the same spectrum analyzer. Both single ended and double ended tests have been performed and the results were consistent with each other. A picture of the frequency domain test setup to measure the noise figure of the multiplier is shown in Fig. 23.

The measured NF varies from 14.4 to 16.9 dB over the RF range from 3 to 4.5 GHz (LO frequency is 5 GHz, i.e. high-side injection), cables and baluns inclusive, as in Fig. 24.

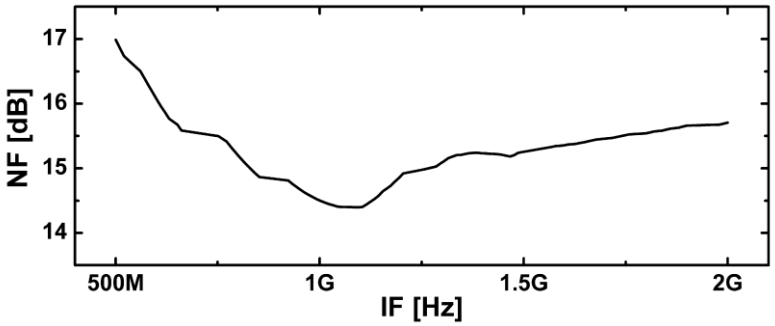


*Fig. 24 – The double side band (DSB) NF of the multiplier over the RF range from 3 to 4.5 GHz with LO frequency equal to 5 GHz.*

It is worth mentioning that, due to the bandwidth limitations (1-12 GHz) of the baluns, the accuracy of this measurement is limited to IF>1 GHz.

## *2.4 Comparison with the state of the art*

Not many works on UWB analog multiplier can be found in literature. Some of those report adequate performance for their possible application to the SoC UWB radar. Among those, only a few are completed by measurement results ([51-53]). For convenience, they are described hereinafter.

In [51] a low power RF multiplier with ultra-wide signal response band is presented for ultra-wide band system applications such as an UWB demodulator (FM-UWB) or RF-correlator (impulse-radio). The CMOS multiplier presented in [51] (Fig. 25) is essentially a transconductance based multiplier where transistors M1, M2, M3 and M4 operates in the linear region while M5, M6, M7 and M8 operates in the saturated region. Analytical analysis is presented together with simulation and measurement results. The practical circuit is implemented using a 0.25 µm CMOS process from UMC. The test results show an average gain of 22.5 $dBV^{-1}$ at 1.2 GHz and 20.8 $dBV^{-1}$ at 3 GHz. Across a full bandwidth of more than 700 MHz the design provides high in-band gain flatness. The circuit consumes a total of 1.3 mA from a 2.5-V supply. The total circuit area is 200×300 $\mu m^2$.

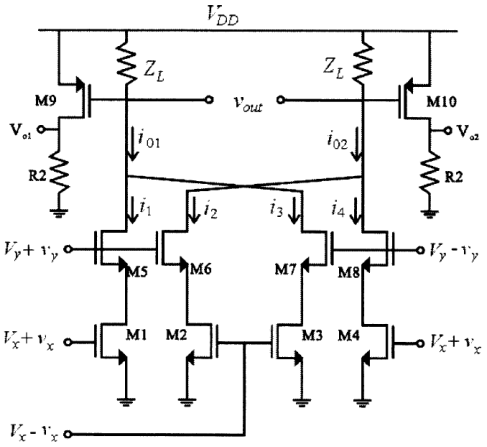


*Fig. 25 – Transconductance based CMOS multiplier proposed in [51].*

In [52] an analog correlator circuit for pulse-based ultra-wideband (UWB) communication is presented. VGA-like architecture is chosen for the multiplier in the correlator. The Gilbert cell based multiplier presented in [52] (Fig. 26) uses a dynamic bias control (DBC) circuitry that makes it work only when the local pulse is on, In this way the contribution from the multiplier offset, integrator leakage and power consumption are all reduced. Analysis and measurement of the correlator are presented. This correlator chip has been fabricated in a commercial 0.18 µm CMOS technology. Simulation shows this correlator is quite resistant to offsets

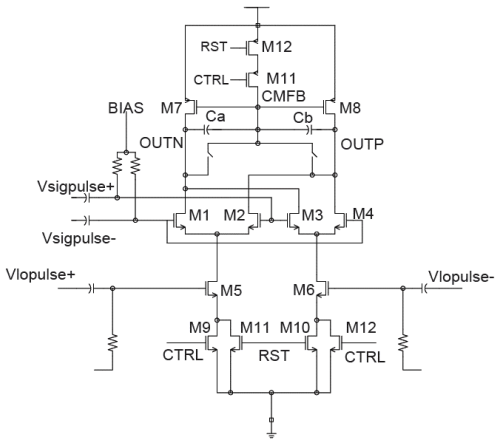


*Fig. 26 – Correlator with multiplier offset reduction and reset switch proposed in [52]. The multiplier is based on the Gilbert cell topology.*

from both input ports. Measurement demonstrates good linearity and gain performance with power consumption of only 5.2 mW. 1-dB compression point is 7 dBm for the input pulse port and 8 dBm for the local pulse port. Power Gain is 8.9 dB at 100 mV-pp Local pulse, IF= 100 MHz, LO= 5 GHz.

In [53] a fully integrated low-power broadband multiplier-based correlator for a 3.1–10.6-GHz full band IR-UWB receiver in 0.18μm CMOS is presented. The double-balance multiplier in [53] (Fig. 27) consists of a UWB multiplier core, two UWB pulse generators, single-ended-to-differential-ended converter, a first-order *RC* integrator with a 200-MHz bandwidth, and a buffer. Measurement results confirm desired correlation-type demodulation and correlation functions with a conversion gain of 11.03 dB, noise figure of 15.7 dB, very low power consumption of 52 mW and a 1-dB compression point better than −0.8 dBm over a 7.5-GHz bandwidth.

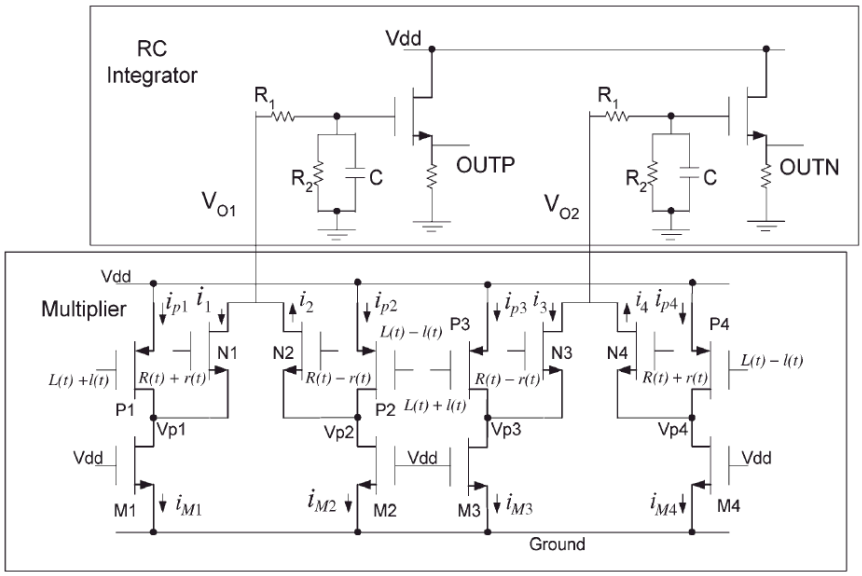


*Fig. 27 –Schematics for the UWB correlator (Multiplier and RC integrator) proposed in [53]. The multiplier is based on a double-balanced topology.*

Table II reports the summary of the performance for a comparison with the SoA. Note the advances of this work in terms of $P_C$, NF, $P_{1dB}$ and area on die. Moreover, note that only [53] reports also noise and linearity performance. From Table II it is worth emphasizing two major aspects. The former is the significant improvement in terms of $P_{1dB}$ (+4.5 and +6 dB for P and Q inputs, respectively). Considering that high linearity range and low power consumption are contradictory requirements, it is important to note that such $P_{1dB}$ are achieved with the lowest supply voltage and $P_C$ (only 0.9 against 3.25 mW of the SoA), i.e. 28% only. The latter is that this design achieves also the lowest NF, in spite of the lowest $P_C$ and the common-gate input stage.

TABLE II: PERFORMANCE SUMMARY AND COMPARISON WITH THE SOA

| Reference | [51] | [52] | [53] | This work |
|---|---|---|---|---|
| Node | 0.25 µm | 0.18 µm | 0.18 µm | 90 nm |
| Area [µm$^2$] | 200×300 | 230×170 | - | 150×200 |
| $P_C$ [mW] | 3.25* | 5.2 | 52 | 3.7 (0.9*) |
| Supply [V] | 2.5 | 1.8 | 1.8 | 1.2 |
| $B_{3dB}$ [GHz] | 0.7 - 3 | - | 3 - 10.6 | 0 - 5.6 |
| $G_C$ [dB @ GHz] | 22.5 @ 1.2 (voltage) | 8.9 @ 4.9 (power) | 11 @ 3.1 - 10.6 (-) | 12.7 @ 2 - 4 (voltage) |
| NF [dB @ GHz] | - | - | 15.7 @ 3 (min) | 14.36 @ 4 (min) |
| $P_{1dB}$ (input) | - | - | < -8 dBm | -3.5 dBm (P) -2 dBm (Q) |

* multiplier core only (bias circuitry excluded)

## *2.5 Summary*

A fully differential wideband multiplier has been designed in 90nm CMOS by implementing p-MOSFET common-gate differential pair and Gilbert's quad as input stages. The design criteria have been presented and discussed. The input-output energy ratio has been introduced as a time-domain metric used to fine tune the circuit design. The test-chip area is 560×700 µm$^2$. The overall power consumption amounts to 3.7 mW from a 1.2-V power supply. The measurements on test-chips show an Input Output Energy Ratio equal to 2 in the case of input monocycle pulses with duration time of 700 ps, conversion gain of 12.7 dB at intermediate frequency in the range from 0.001 to 10 MHz for input tones in the range from 2 to 4 GHz, noise figure of 14.4 dB (min) and compression point of -3.5 and -2 dBm for the two inputs.

The experimental characterizations of the test-chips confirm the advances of the performance with respect to the state of the art, especially in terms of power consumption, linearity and noise. These benefits of the proposed circuit solution allow the implementation of efficient radiofrequency integrated systems for emerging UWB applications.

# 3. CMOS SOC UWB PULSE RADAR

This chapter reports a summary of the major results achieved by the research group for the SoC UWB pulse radar. Therefore, this chapter offers the opportunity to validate the effectiveness of the novel analog multiplier design reported in the previous Chapter 2 and which is the objective of this PhD thesis.

## *3.1 Summary on building blocks*

For reasons of self-consistency, this paragraph reports a summary of the major results achieved by the research group regarding the implementation of the most critical building blocks of the radar.

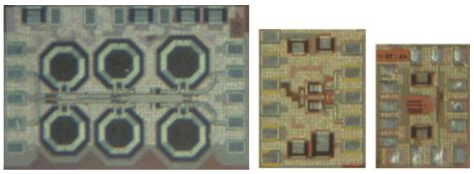

*a)* *b)* *c)*

*Fig. 28 – Pictures of the main building blocks of the pulse radar: a) LNA, b) Pulse Generator and c) Delay Generator.*

In addition to the analog multiplier reported previously in Chapter 2, the other most critical building blocks are the low noise amplifier (LNA) [35], pulse generator (PG) [36] the programmable delay generator (DG) [37], and integrator [59]. This section reports the major results achieved for the implementations of these blocks that have been realized as stand-alone circuits in 90nm CMOS technology by ST-Microelectronics (see Fig. 28) and then co-integrated for the overall system-on-chip implementation.

A summary of the performance of the critical building blocks is reported in the following subsections.

### 3.1.1 LNA

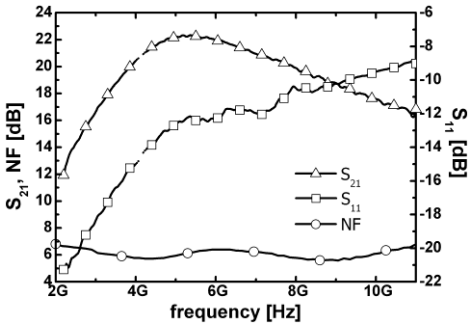


*Fig. 29 – Measured LNA performance. The noise figure (NF) includes the noise contribution of the test-circuitry (UWB baluns and cables).*

The ultra-wide-band low noise amplifier (Fig. 28-a) consists of a common gate stage which realizes a wideband input impedance matching to the source impedance of the receiver (i.e. the antenna), and two subsequent common source stages which increase the overall gain of the amplifier [35]. The LNA consumes 34.8 mW from a 1.2 V voltage supply. Measurements show a transducer gain of 22.7 dB at 5.2 GHz, a -3 dB band from 3.56 and 8.46 GHz, an input reflection coefficient lower than -10.5 dB in band, and an input-referred 1dB compression point of -19.7 dBm, in very good agreement with the post-layout simulation results. The measured noise figure is close to 6.5 dB (including losses due to UWB baluns,

probes and cables) in all the 3.1-10.6 GHz frequency range. The measured $S_{21}$ and $S_{11}$ parameters and noise figure are shown in Fig. 29.

### 3.1.2 Monocycle pulse generator

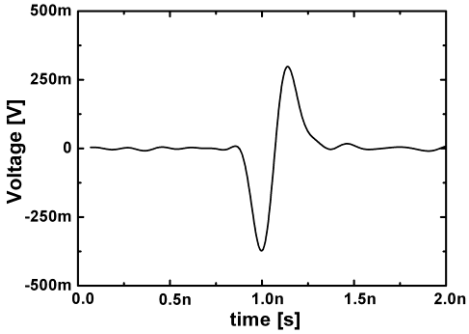


*Fig. 30 – Measured output monocycle pulse of the pulse generator.*

The pulse generator (see Fig. 28-b) provides a monocycle pulse on a 100Ω differential load (i.e. the antenna) when activated by the negative edge of a digital signal (i.e. a command signal occurring at the pulse repetition frequency) provided by the micro-controller (μC). The schematic and the operating principle of the pulse generator are detailed in [36]. Duration time and peak-to-peak amplitude of the pulses are respectively 430 ps and 660 mVpp (including the loss of microprobes and cables). This value corresponds to around 900 mVpp on chip. The power consumption is 19.8 mW from a 1.2-V power supply. The measured differential output voltage of the pulse generator is shown in Fig. 30.

### 3.1.3 Delay generator

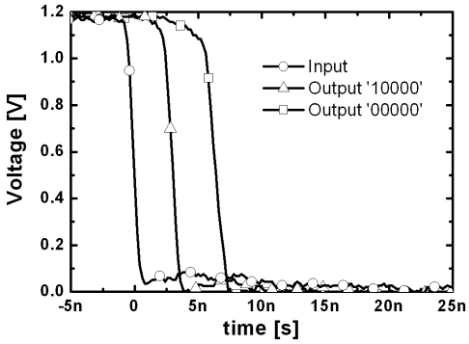


*Fig. 31 – Input and output voltage (measured) of the delay generator for two different values of the input vector, captured by an oscilloscope with input impedance of 1 MΩ in parallel with 13 pF (in addition to the parasitic capacitances of the cables).*

The Delay Generator (Fig. 28-c) provides a 5-bit digitally programmable delay for the negative edge of the digital signal that activates the pulse generator. The design has been optimized to drive properly the capacitive input impedance of the pulse generator (close to 40 fF). Schematic and operating principle are reported in [37, 59]. Simulated results show that it can provide a delay from 1 ns to 3.5 ns. The result of the measurements with an oscilloscope (Tektronix TDS 3054B) is shown in Fig. 31. The range of obtainable delays is wider than the simulated one, because the input capacitance of the oscilloscope is equal to 13 pF, while the delay generator has been designed for a 40 fF load. This has been proved by means of accurate circuit simulations.

### 3.1.4 Integrator

The integrator consists of a 3-stage amplifier with RC feedback and output buffer. The stages use identical differential pair amplifiers. The voltage gain is 58 dB and $B_{3dB}$=147 Hz (post-layout simulations).

## *3.2 SoC UWB Radar: feasibility and performance evaluation*

The material presented in this section was reported in [59].

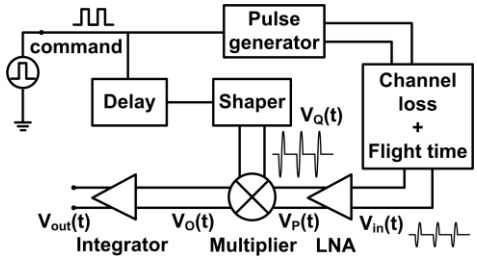


*Fig. 32 – Signal flow through the radar.*

The post-measurement evaluation of the feasibility and performance of the whole system have been carried out by means of accurate and extensive transient simulations, which take also into account the measured performance of the most critical blocks where available. The signal flow through the radar block scheme is shown in Fig. 32. The pulse generator and the shaper are activated by the negative edge of a digital signal (*command* in Fig. 32). The pulse generator output signal has been attenuated of 80 dB (according to the measured channel loss through the human chest [33, 34]) before being applied to the input of the LNA. Therefore the output monocycle pulse of almost 900 mVpp reduces to 90 µVpp at the input of the LNA. A channel delay of two nanoseconds has also been included in order to emulate the flight time of the pulse from the transmitter to the receiver.

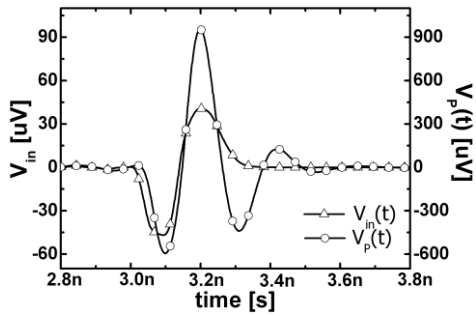


*Fig. 33 – Input and output signals ($V_{in}$ and $V_1$, respectively) of the LNA (simulated in accordance with the measured performance of LNA, pulse generator, and intra-body channel).*

The input and output signals of the LNA ($V_{in}$ and $V_P$, respectively) are shown in Fig. 33. The signal $V_P$ is one input of the multiplier while the other is the output signal of the shaper $V_Q$. With a proper choice of the programming bits of the delay generator, the activation of the shaper has been delayed by two nanoseconds in order to align in time the two input pulse signals of the multiplier. In this way, the subsequent result of the correlation is maximized.

In the final system, this delay adjustment to the specific physiology of each subject under monitoring (i.e. skin-hearth distance) will be carried out automatically by the µC.

The output and two input signals of the multiplier are reported in Fig. 34. Note that when the two input signals ($V_P$ and $V_Q$) reach their peak values, the output of the UWB multiplier ($V_O$) is conformal to the expectations. By acting on the

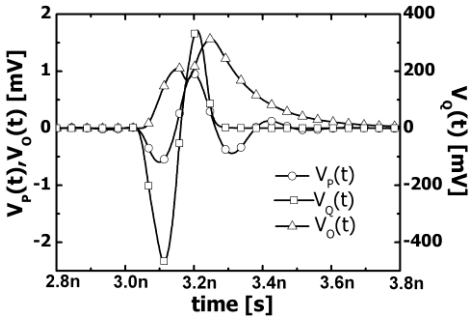


*Fig. 34 – Input ($V_1$ and $V_2$) and output ($V_3$) signals of the multiplier (simulated in accordance with the performance measured for LNA, pulse generator, delay generator, and intra-body channel).*

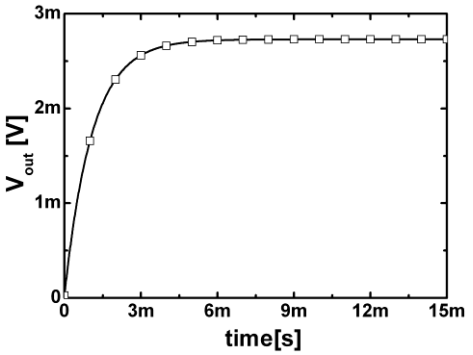


*Fig. 35 – Transient response of the radar receiver with PRF equal to 10 MHz.*

*command* signal, the system can be tested for different values of pulse repetition frequency (PRF). The output signal of the integrator ($V_{out}$), resulting from the post-layout simulation with PRF equal to 10 MHz, is shown in Fig. 35. Slow variations of the integrator steady-state output voltage are expected when a slow moving object is under observation. In particular, when there is no overlapping between the two input signals the result of the multiplication is null and thus the output of the integrator decays. The steady-state value of the output signal is about 2.7 mV.

Thanks to the implementation and testing of the building blocks of the radar, it has been possible to carry out a post-measurement review of the feasibility study. The simulation results of the overall radar system confirm the capability of the SoC pulse radar to detect the heart movement.

## *3.3 SoC UWB Radar: experimental results*

This paragraph reports the experimental results achieved by the research group for the SoC UWB pulse radar applied to the contact-less detection of respiratory rate.

The material presented in this section was reported in [60]

In order to underline the impact of the overall research project, it is worth mentioning that with respect to continuous wave (CW) radars [19], UWB radar transceivers present a lower circuit complexity since no frequency conversions are required, leading to lower power consumption ($P_C$) for a longer battery autonomy. Moreover, in spite of the implementations of efficient building blocks [35, 36, 61], UWB radar front-ends, fully integrated in a single silicon die, tested and working, have not been reported yet in the literature.

### 3.3.1 Test scenario

With reference to Fig. 36, the delay can be varied in order to span the range of interest and identify the target (*ranging mode*, RM). This can be done by acting on the 5-bit programmable delay generator (DG). By varying the bias current, the DG can provide delays in the range from 1 up to 30 ns. When the target is detected, the delay can be fixed in order to monitor a fixed range gate (*tracking mode*, TM). Since vital signs vary within a few Hertz, an integrator 3-dB band ($B_{3dB}$) of 100 Hz allows an accurate detection. The average of a large number of pulses (in the order $f_{PR}/B_{3dB}$) allows us to increase the $SNR_{out}$ (e.g. $10^5$ pulses for $f_{PR}$ = 10 MHz).

Therefore, the output voltage is directly sensitive to the target movements, e.g. the chest movements due to the pulmonary activity in case of respiratory rate monitoring.

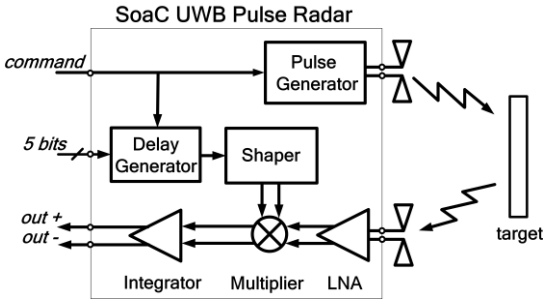


*Fig. 36 – Block diagram of the SoC UWB radar front-end.*

All the circuits have been designed according to the specifications derived by the feasibility study [30]. They have fully differential topologies for better immunity to EMI and noise, and linearity. The test-chip layout and micrograph are reported in Fig. 37.

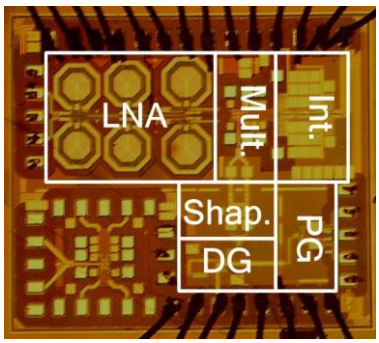


*Fig. 37 – Micrograph of the radar testchip. Die size: 1.5×1.3 mm$^2$ (pads are ESD protected). This includes also the Multiplier as stand-alone device.*

The UWB radar sensor has been tested in three different experimental test setups (TS1, TS2 and TS3).

### 3.3.2 TS1: chip functionality

The system has been first tested to verify the chip functionality. The overall power consumption amounts to 73.2 mW from a 1.2-V power supply. In table III the power consumptions related to each building block are reported. The overall $P_C$ is less than CW radars for similar applications (e.g. >80mW [19]).

TABLE III: $P_C$ OF THE SINGLE BUILDING BLOCKS (BIAS INCLUSIVE)

| Block | PG | LNA | Multiplier | Integrator | Shaper | DG |
|---|---|---|---|---|---|---|
| $P_C$ [mW] | 19.8 | 34.8 | 3.7 | 1.1 | 13.8 | <0.1 |

In TS1, we tested the radar test-chip only (no antennas). Pictures of TS1 are shown in Fig. 38. A shielded manual prober has been used to minimize the influence of external noise. All instruments were outside and were connected to the inside through triaxial connectors on the side of the shield.

The command signal comes from a function generator (HP8116A). The outputs of the receiver chain (i.e. the output of the integrator) are connected to a digital oscilloscope (DSO3202A by Agilent). The bias current of the DG is controlled by a waveform generator (33250A by Agilent). In this way the movement of the object can be simulated.

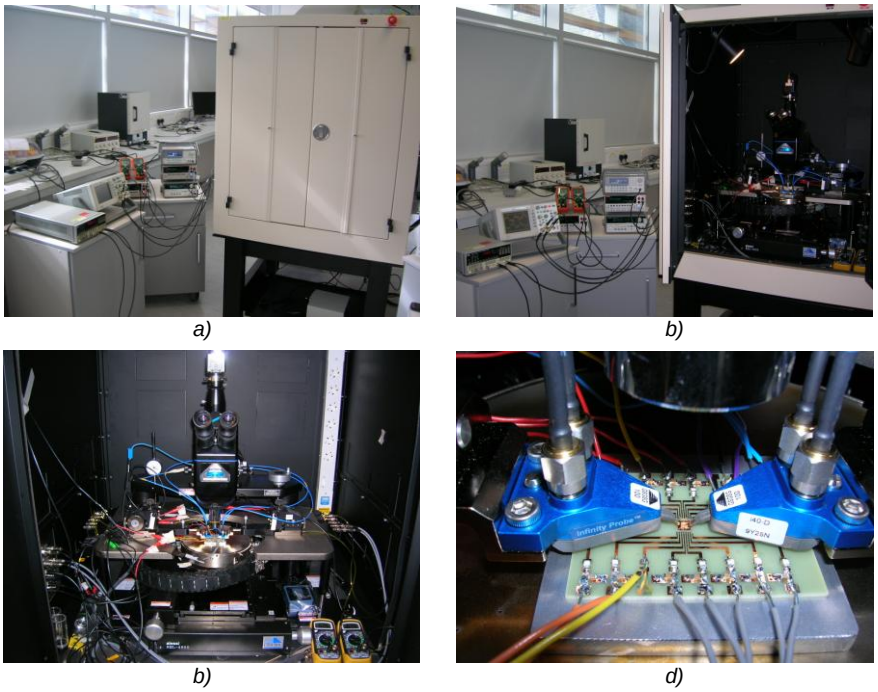

*a)* *b)*

*b)* *d)*

*Fig. 38 – Pictures of TS1: a) and b) complete view of the shielded manual prober and instruments aside on the left, b) inside of the shielded manual prober, c) detail of the test board with RF microprobes.*

A scheme of the TS1 is shown in Fig. 39. The PG output is connected to the LNA input by means of microprobes, cables and attenuators. The propagation delay of cables is fixed (~8ns), which corresponds to a static target.

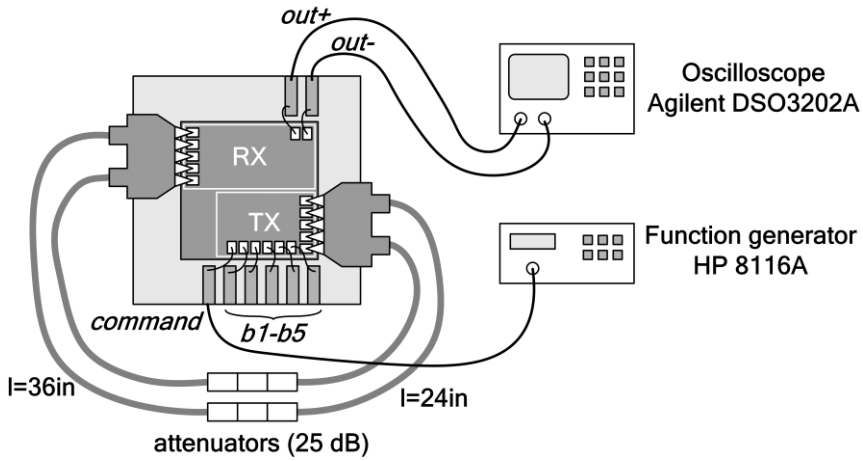


*Fig. 39 – Scheme diagram for TS1.*

The output voltage for RM is shown in Fig. 40. DG is driven by a ramp in order to span the range of interest (around 8ns).

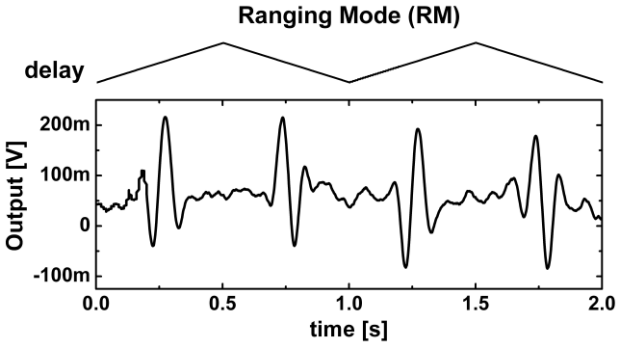


*Fig. 40 – Output voltage for RM ($f_{PR}$=40MHz).*

The output voltage for TM is shown in Fig. 41. The target movement is emulated by driving the DG with a square waveform corresponding to full and no correlations between echoes and on-chip replicas, as in case (a) and case (c) of Fig. 19.

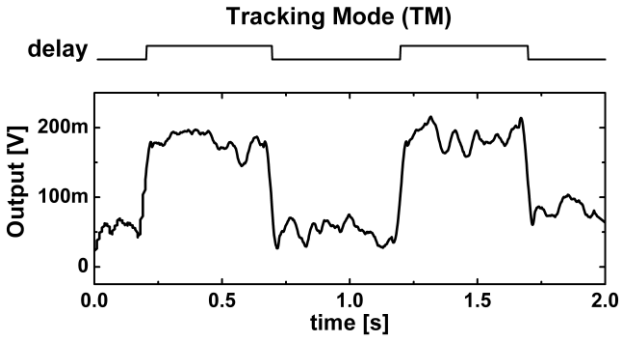


*Fig. 41 – Output voltage for TM ($f_{PR}$=40MHz).*

These results demonstrate that the test-chip works properly. Note that the dc offset (~50mV), which can be eliminated by means of digital processing, is not an issue for this application aimed at detecting the movement rate.

### 3.3.3 TS2: radar functionality

Figure 42-a shows TS2, in which the radar test-chip (packaged in QFN32) is mounted on a test-board including the antennas (2.3 dBi at 3.5 GHz, |S11|< -10 dB in the band 2.8 to 5.4 GHz, which covers the range of interest 3 to 5 GHz). The target is made of a 0.5 cm-thick board covered by an aluminium foil. In TS2, the radar detected 3 targets with different areas (26×26, 13×26 and 13×13 $cm^2$) for movements (front-back) up to d=2 cm around a distance (D) up to 70 cm.

Figure 42-b reports the output voltage for the target of area 26×26 $cm^2$ (d=2 cm, D=70 cm). The energy consumption per pulse received is 59.4 mW×0.6 ns = 36 pJ ($t_D$ of the echo captured by the antenna is ~0.6ns).

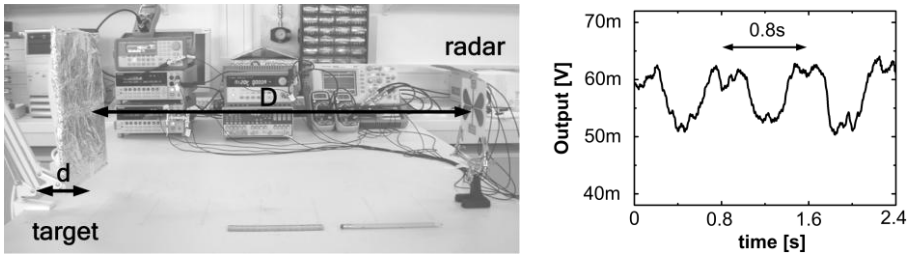


*a)* *b)*

*Fig. 42 – a) TS2 and b) output voltage at maximum distance D=70 cm for minimum target movement range d=2 cm ($f_{PR}$ =40 MHz).*

### 3.3.4 TS3: respiration rate detection

Figure 43-a shows TS3, in which the radar detects the respiratory rate (~0.5 Hz) of the person under test placed at D=25 cm (Fig. 43-b).

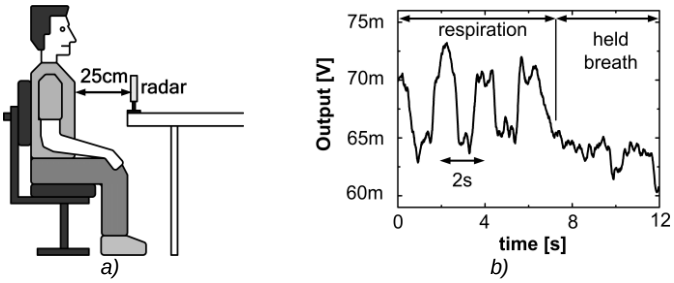


*Fig. 43 – a) TS3 and b) output voltage at distance D=25 cm ($f_{PR}$ =40 MHz).*

All these results demonstrate that the UWB radar sensor proposed detects properly the targets in the operating scenarios.

## *3.4 Summary*

A UWB radar sensor for biomedical application has been implemented in 90nm CMOS. The transceiver is made of a transmitter based on a UWB monocycle pulse generator and a correlation receiver based on the chain of UWB LNA, UWB multiplier and integrator. The test-chip area is 1.5×1.3mm$^2$. The overall power consumption amounts to 73.2 mW from a 1.2-V power supply.

The measurements on test-chips demonstrate that the proposed UWB radar sensor works properly and can detect a moving target made of a 0.5 cm-thick board covered by an aluminium foil at a maximum distance of 70 cm for minimum target movements in the range of 2 cm.

Moreover the bio-sensing capability of the radar has been proved with the detection of the respiratory rate (~0.5 Hz) of a person placed at a distance of 25 cm.

This work presents the first implementation, including experimental evidences, of a SoC UWB pulse radar front-end based on a correlation receiver, in 90nm CMOS technology by STM.

## REFERENCES


1. "Extending the scope of ICT at the Crossroads with life sciences", 7th framework workshop, Bruxelless, Oct. 2004.
2. Romano M., et al., "Minimally Invasive and Noninvasive Hemodynamic Monitoring of the Cardiovascular System: Available Options and Future Perspectives", *Current Cardiology Reviews*, Vol. 2, Is. 1, Feb. 2006, pp. 37-39.
3. Huasong C., Leung V., Chow C., Chan H., "Enabling technologies for wireless body area networks: A survey and outlook", *IEEE Communications Magazine*, Vol. 47, Is. 12, Dec. 2009, pp. 84-93.
4. Jovanov E., Milenkovic A., Otto C. and Piet C de Groen, "A wireless body area network of intelligent motion sensors for computer assisted physical rehabilitation", *Journal of NeuroEngineering and Rehabilitation*, Online Journal, Vol. 2, Mar. 2005. Available: http://www.jneuroengrehab.com/content/2/1/6
5. Tia Gao, Massey T., Selavo L., Crawford D., Bor-rong Chen, Lorincz K., Shnayder V., Hauenstein L., Dabiri F., Jeng J., Chanmugam A., White D., Sarrafzadeh M., Welsh M., "The advanced health and disaster aid network: a light-weight wireless medical system for triage", *IEEE Transactions on Biomedical Circuits and Systems*, Vol. 1, Is. 3, Sept. 2007, pp. 203-216.
6. Benini L., Farella E., Guiducci C., "Wireless sensor networks: Enabling technology for ambient intelligence", *Microelectronics Journal*, Vol. 37, Is. 12, Dec. 2006, pp. 1639-1649
7. CardioLabs, [Online]. Available: http://www.cardiolabs.com
8. CardioNet, [Online]. Available: http://www.cardionet.com
9. TurnerMedical.com, [Online]. Available: http://www.turnermedical.com
10. Milenkovic A., Otto C., Jovanov E., "Wireless sensor networks for personal health monitoring: Issues and an implementation", *Computer Communications*, Vol. 29, Is. 13-14, Wireless Sensor Networks and Wired/Wireless Internet Communications, 21 Aug. 2006, pp. 2521-2533.
11. ProeTEX, Project FP6-2004-IST-4-026987, [Online]. Available: www.proetex.org
12. Mincica M., Pepe D., Tognetti A., Lanatà A., De Rossi D., Zito D., "Enabling technology for heart health wireless assistance", Proceeding of the 12th IEEE International Conference on e-Health Networking Applications and Services (Healthcom), Lion, France, 1-3 July 2010, pp. 36-42.
13. Mingqi C., Boric-Lubecke O., Lubecke V.M., "0.5um CMOS implementation of analog heart-rate extraction with a robust peak detector", *IEEE Transactions on Instrumentation and Measurement*, Vol. 57, Is. 4, Apr. 2008, pp.690 – 698.
14. Dr Fearnley SJ, "Pulse Oximetry", *World Anesthesia*, Online Journal. Is. 5, Article 2, 1995. Available: http://www.nda.ox.ac.uk/wfsa/html/u05/u05_003.htm
15. Lin J.C., "Microwave sensing of physiological movement and volume change: a review", *Bioelectromagnetics*, Vol. 13, 1992., pp. 557–565
16. McEwan T.E., "Body monitoring and imaging apparatus and method", U.S. Patent 5,573,012, Nov. 12, 1996.
17. Immoreev I. J. and Samkov S.V., "Ultra-wideband (UWB) radar for remote measuring of mainparameters of patient's vital activity", *Radio Physics and Radio Astronomy*, Vol. 7, Is. 4, Dec. 2002, pp. 404–407.

18. Staderini E.M., "UWB radars in medicine", *IEEE Aerospace and Electronic Systems Magazine*, Vol. 17, Is. 1, Jan. 2002, pp. 13–18.
19. Droitcour A.D., Boric-Lubecke O., Lubecke V.M., Jenshan Lin, "0.25 um CMOS and BiCMOS single-chip direct-conversion Doppler radars for remote sensing of vital signs", Digest of Technical Papers in 2002 IEEE International Solid-State Circuits Conference. ISSCC 2002. Vol. 1, 2002, pp. 348-349.
20. Droitcurt A.D., Boric-Lubecke O., Lubecke V.M., Lin J., and Kovacs G.T.A., "Range correlation and I/Q performance benefits in single chip silicon radars for noncontact cardiopulmonary monitoring", *IEEE Transactions on Microwave Theory and Techniques*, Vol. 52, Is. 3, 2004, pp. 838 - 848.
21. Li C., Xiao Y., Lin J., "A 5 GHz Double-Sideband Radar Sensor Chip in 0.18µm CMOS for Non-Contact Vital Sign Detection", *IEEE Microwave and Wireless Components Letters*, Vol. 18, Is. 7, July 2008, pp. 494-496.
22. Changzhi Li, Xiaogang Yu, Chien-Ming Lee, Dong Li, Lixin Ran, Jenshan Lin, "High-Sensitivity Software-Configurable 5.8-GHz Radar Sensor Receiver Chip in 0.13-um CMOS for Noncontact Vital Sign Detection", *IEEE Transactions on Microwave Theory and Techniques*, Vol. 58, Is. 5, 2010, pp. 1410-1419.
23. Wong A., Kong-Pang Pun, Yuan-Ting Zhang, Hung K., "A near-infrared heart rate measurement IC with very low cutoff frequency using current steering technique", *IEEE Transactions on Circuits and Systems I: Regular Papers*, Vol. 52, 2005, pp. 2642-2647.
24. Phan D. H., Bonnet S., Guillemaud R., Castelli E., Pham Thi N. Y., "Estimation of respiratory waveform and heart rate using an accelerometer", Proceeding of the 30th Annual International Conference of the IEEE Engineering in Medicine and Biology Society, 2008. EMBS 2008, Vancouver, Canada, Aug. 2008, pp. 4916-4919.
25. Mukai K., Yonezawa Y. Ogawa H., Maki H., Caldwell W.M., "A remote monitor of bed patient cardiac vibration, respiration and movement", Proceeding of the Annual International Conference of the IEEE Engineering in Medicine and Biology Society, 2009. EMBC 2009, Minneapolis, MN, USA, 3-6 Sept. 2009, pp. 5191-519.
26. Wang X., Dinh A., Teng D., Chen L., Ko S.B., Shi Y., Basran J., Bello-Hass V.D., "Impulse based range-gated UWB wireless transceiver IC in 90nm CMOS for medical sensing applications and communications", Proceeding of the IEEE International Conference on Ultra-Wideband, 2009. ICUWB 2009, Vancouver, BC, Canada, 9-11 Sept. 2009, pp. 194-199.
27. Zito D., Pepe D., Neri B., De Rossi D., Lanata A., Tognetti A., Scilingo E.P., "Wearable system-on-a-chip UWB radar for health care and its application to the safety improvement of emergency operators", Proceeding of the 29th International Conference of the IEEE Engineering in Medicine and Biology Society, 2007. EMBS 2007, Lyon, France, Aug. 23-26 2007, pp. 2651–2654.
28. "New public safety applications and broadband internet access among uses envisioned by FCC authorization of ultra-wideband technology", Federal Communications Commission, 2002. [Online]. Available: http://www.fcc.gov/Bureaus/Engineering_Technology/News_Releases/2002/nret0203.html
29. "Etsi ultra wide band", European Telecommunications Standards Institute (ETSI), 2008. [Online]. Available: http://www.etsi.org/WebSite/Technologies/UltraWideBand.aspx

30. Zito D., Pepe D., Neri B., Zito F., De Rossi D., and Lanatà A., "Feasibility Study and Design of a Wearable System-on-a-Chip Pulse Radar for Contact-less Cardiopulmonary Monitoring", *International Journal of Telemedicine and Applications*, Indawi Publishing Corp., Vol. 2008, Published online 2008 March 17, pp.1-10.
31. Gabriel C. and Gabriel S., "Compilation of the dielectric properties of body tissues at rf and microwave frequencies", 2002. [Online]. Available: http://www.brooks.af.mil/AFRL/HED/hedr/reports/dielectric/home.html
32. Andreuccetti D., Fossi R., and Petrucci C., "Calculation of the dielectric properties of body tissues in the frequency range 10Hz-100GHz", 2002.
33. Zito D., Pepe D., Mincica M., Zito F., De Rossi D., Lanata A., Scilingo E. P., Tognetti A., "Wearable system-on-a-chip UWB radar for contact-less cardio-pulmonary monitoring: present status", Proceeding of the 30th Annual International Conference of the IEEE Engineering in Medicine and Biology Society, 2008. EMBS 2008, Vancouver, Canada, Aug. 2008, pp. 5274-5277.
34. Zasowski T., Althaus F., Stager M., Wittneben A., Troster G., "UWB for noninvasive wireless body area networks: channel measurements and results", Proceeding of the IEEE Conference on Ultra Wideband Systems and Technologies, Reston, Virginia, 16-19 Nov. 2003, pp. 285-289.
35. Pepe D., Zito D., "22.7 dB gain -19.7 dBm ICP1dB UWB CMOS LNA", *IEEE Transactions on Circuits and Systems II*, Vol. 56, Is. 9, Sep. 2009, pp. 689-693.
36. Zito F., Pepe D., Zito D., "UWB CMOS Monocycle Pulse Generator", *IEEE Transactions on Circuits and Systems I: Regular Papers*, Vol. 57, Is. 10, Oct. 2010, pp. 2654 - 2664.
37. Zito F., Zito D. and Pepe D., "UWB 3.1-10.6 GHz CMOS transmitter for system-on-a-chip nano-power pulse radars", Proceeding of the IEEE PhD Research in Microelectronics and Electronics Conference, 2007. PRIME 2007, Bordeaux, France, 2-5 July 2007, pp. 189-192.
38. Mincica M., Pepe D., Giordano A., Zito D., "CMOS correlation receiver for UWB pulse radar", Proceeding of the IEEE PhD Research in Microelectronics and Electronics Conference, 2009. PRIME 2009, Cork, Ireland, 12-17 July 2009, pp. 356-359.
39. Paradiso R., "Knitted textile for the monitoring of vital signals," WO2005053532, 2005.
40. Faetti T., Lanatà A., Nardini E., Scilingo E. P., and De Rossi D., "A comparative evaluation of different techniques for ambulatory monitoring of respiratory rate", International Workshop on Wearable Micro and Nanosystems for Personalised Health (pHealth2008), 2008.
41. Oliveira A., Gehin C., Delhomme G., Dittmar A., McAdams E., "Thermal Parameters Measurement on Fire Fighter During Intense Fire Exposition", Proceedings of the 31st Annual International Conference of the IEEE Engineering in Medicine and Biology Society, 2009. EMBC 2009, Minneapolis, MN, USA, 3-6 Sept. 2009, pp. 4128 – 4131.
42. Anania G., Tognetti A., Carbonaro N., Tesconi M., Cutolo F., Zupone G., De Rossi D., "Development of a novel algorithm for human fall detection using wearable sensors", IEEE Sensors 2008, Lecce, Italy, 26-29 Oct. 2008, pp. 1336-1339.

43. Tognetti A., Bartelesi R., Lorussi F., and De Rossi D., "Body segment position reconstruction and posture classification by smart textiles", *Transactions of the Institute of Measurement and Control*, Vol. 29, Is. 3-4, Aug. 2007, pp. 215-253.
44. Amato G., Caruso A., Chessa S., "Application–Driven, Energy–Efficient Communication in Wireless Sensor Networks", *Computer Communications*, Vol. 32, Is. 5, March 2009, pp. 896–906.
45. Teo T.H., Gopalakrishnan P.K., Hwan Y.S., Qian X.B., Haridas K., Pang C.Y., Je M., "A 700-μW single-chip IC for wireless continuous-time health monitoring in 0.18-μm CMOS", Proceeding of the IEEE Asian Solid-State Circuits Conference 2009. A-SSCC 2009, Taipei, 16-18 Nov. 2009, pp. 361-364.
46. Karapistoli E., Pavlidou F.-N., Graugopoulus I., Tsetsinas I., "An Overview of the IEEE 802.15.4a Standard", *IEEE Communication Magazine*, Vol. 48, Is. 1, 2010, pp. 47-53.
47. Pelissier M., Morche D., Vincent P., "Super-Regenerative Architecture for UWB Pulse Detection: From Theory to RF Front-End Design", *IEEE Transactions on Circuits and Systems I*, Vol. 56, Is. 7, July 2009, pp. 1500-1512.
48. Gerosa A., Solda S., Bevilacqua A., Vogrig D., Neviani A., "An Energy-Detector for Noncoherent Impulse-Radio UWB Receivers", *IEEE Transactions on Circuits and Systems I*, Vol. 56, Is. 5, May 2009, pp. 1030-1040.
49. Reja M., Moez K., Filanovsky I., "An Area-Efficient Multistage 3.0 to 8.5 GHz CMOS UWB LNA Using Tunable Active Inductors", *IEEE Transactions on Circuits and Systems II*, Vol. 57, Is. 8, Aug. 2010, pp. 587-591.
50. Mincica M., Zito D., Pepe D., "CMOS UWB analog multiplier", *IEEE Transactions on Circuits and Systems-II: Express Briefs*, submitted Dec. 7, 2010.
51. Tian T., Chih-An L., Jensen O.K., Mikkelsen J.H., Larsen T., "A 0.25um CMOS Low Power RF Multiplier for Ultra-wide Band System Applications", Proceeding of the 2005 IEEE European Electron Devices Solid-State Circuits Conference. EDSSC 2005, 19-21 Dec. 2005, pp. 221-224.
52. Shen D., Fujiang L., Wooi Gan Y., "An analog correlator with dynamic bias control for pulse based UWB receiver in 0.18um CMOS technology", Proceeding of the 2006 IEEE Radio Frequency Integrated Circuits (RFIC) Symposium, 11-13 June 2006, pp.1-4.
53. Haolu X., Xin W., Lin L., He T., Qiang F., Hui Z., Shijun W., Fei Y., W. Albert, Yumei Z., Bo Q., "A 52-mW 3.1-10.6GHz Fully Integrated Correlator for IR-UWB Transceivers in 0.18um CMOS", *IEEE Transactions on Industrial Electronics*, Vol. 57, Is. 5, May 2010, pp. 1546-1554.
54. Jeong-Bae S., Jong-Ha K., Hyuk S., Tae-Yeoul Y., "A Low-Power and High-Gain Mixer for UWB Systems", *IEEE Microwave and Wireless Components Letters*, Vol. 18, Is. 5, Dec. 2008, pp. 803-805.
55. Razavi B., **RF Microelectronics**, Prentice Hall, 1998, page 199.
56. Y. Ding and R. Harjani, High-linearity CMOS RF front-end circuits: Springer Verlag, 2005.
57. Lee T., **The design of CMOS radio-frequency integrated circuits**, Cambridge University Press, 2004.
58. Gupta A. K., Dhanasekaran V., Soundarapandian K. and Sanchez-Sinencio E., "Multipath common-mode feedback scheme suitable for high-frequency

two-stage amplifiers", *Electronics Letters*, Vol. 42, Is. 9, Apr. 2006, pp. 499-500.
59. Mincica M., Pepe D., Zito F., Zito D., "Advances in CMOS SoC Radar Sensor for Contactless Cardiac Monitoring", Proceeding of the IEEE PhD Research in Microelectronics and Electronics, 2010. PRIME 2010, Berlin, Germany, 19-21 July 2010, pp. 1-4.
60. Zito D., Pepe D., Mincica M., Zito F., "A 90nm CMOS SoC UWB Pulse for Respiratory Monitoring", accepted as Regular Paper at the IEEE International Solid-State Circuits Conference (ISSCC), San Francisco, CA, 2011, 2 pages.
61. Daly D.C., Mercier P.P., Bhardwaj M., Stone A.L., Voldman J., Levine R.B., Hildebrand J.G., Chandrakasan A.P., "A pulsed UWB receiver SoC for insect motion control", Digest of Technical Papers in 2009 IEEE International Solid-State Circuits Conference. ISSCC 2009, pp. 200–201.